Journal of
Computational and Theoretical Nanoscience
Vol. 3, 167–188, 2006

REVIEW

Nano-Tribological Analysis by Molecular Dynamics Simulation—A Review

L. C. Zhang* and K. Mylvaganam

School of Aerospace, Mechanical and Mechatronic Engineering, The University of Sydney, NSW 2006, Australia

The advent of super computers for large scale atomic simulations and the invention of proximal testing devices such as atomic force microscope, friction force microscope, surface force apparatus, nanoScratcher etc., have led to the development of micro- and nano-tribology. This paper reviews some fundamental concepts and steps involved in molecular dynamics modeling of nanotribology together with some significant aspects such as the mechanisms of wear and friction, the scale effect of asperity contact size on friction, and the deformation induced by two-body and three-body contact sliding on the atomic scale with a focus on the authors' work on copper and silicon. Studies on diamond-copper sliding reveal that there exist four distinct regimes of deformation, and that no-wear deformation can be achieved by using a lower sliding speed, a smaller tip radius and a better lubrication. The variation of the frictional force is a function of contact area in all regimes except that in the cutting regime where the conventional friction law still holds. Investigations into the diamond-silicon sliding show that the amorphous phase transformation is the main deformation in silicon. In a two-body contact sliding, the deformation of silicon falls into no-wear, adhering, ploughing, and cutting regimes while in a three-body sliding it falls into no-wear, condensing, adhering, ploughing and no-damage wear regimes.

Keywords: Nanotribology, Molecular Dynamics, Silicon, Copper, Wear Mechanism, Friction.

CONTENTS

1. INTRODUCTION

Tribology is the science and technology of interacting surfaces in relative motion; it includes the study of lubricants, lubrication, friction and wear.[1] It is an interdisciplinary field that has drawn great interest due to economic as well as to scientific and technological reasons. The objectives of tribology are to control friction, traction, and lubrication and to reduce surface damage such as wear, seizure, and contact fatigue. On the macroscopic scale, tribology tests are carried out with heavy loads applied on substances of relatively large mass. As such wear is inevitable in macro tribology and characterized by bulk properties of the substance. On the other hand, in micro/nano tribology, light loads are applied on substances with small mass and the wear is often on the micron, nanometre or even atomic level. As such the tribological performance of a micro/nano system usually depends more greatly on the surface interaction properties of the system elements in contact sliding. Micro/nano tribological studies are therefore required to understand the interfacial phenomenon in micro/nano structures used in most such systems, e.g., the magnetic storage systems and micro/nano electro mechanical systems (MEMS/NEMS).

Although friction and wear on micro- and nano-scales have been found to be generally smaller than to that on a macro-scale, the adhesion force of a macro scale object is several orders of magnitude smaller than the force of gravity. In contrast, a micro scale object experiences an

*Author to whom correspondence should be addressed.

1546-198X/2006/3/167/022 doi:10.1166/jctn.2006.001

adhesion force over a million times greater than the force of gravity. This is because the adhesion force decreases linearly with size whereas the gravitational force decreases with size cubed.[2] Thus, micro objects adhere to their neighbours or surfaces and this is an obstacle to the miniaturization of components. Reduction in adhesion and friction were brought about by applying principles of surface chemistry and tribology to MEMS & NEMS. Mastrangelo[3] discusses the physical and chemical techniques used to alleviate the problem. Physical schemes were aimed at minimizing contact surface area by eliminating the capillary pull force through methods such as supercritical drying, dry etching, hydrophobic coating etc. Chemical schemes were aimed at minimizing inter-solid surface adhesion through the use of textured surfaces and low-energy monolayer coatings.

With the invention of atomic force microscopy (AFM), NanoIndentor and NanoScratcher, and other instruments such as surface force apparatus (SFA) and scanning tunneling microscope (STM), the study of tribology at micron and nanometer scales has, to some extent, become experimentally possible. Instant deformation is hard to be characterized and high speed sliding is impossible to be carried out on these apparatus. The Atomic Force Microscope introduced in 1985 provided a method for measuring forces on a nano-scale between a probe tip and an engineering surface. It has been used for topographical measurements of surfaces on the nanoscale as well as measuring adhesion and electrostatic force. However, localized deformation, tip-substrate interactions and environmental effects often make the results difficult to reproduce. Subsequent modification of AFM led to the development of Friction Force Microscope (FFM) which is used to measure forces in the scanning direction i.e., the force of friction. An AFM/FFM tip sliding on a surface simulates just one contact whereas at most solid-solid interfaces contact occurs at many asperities. Even so, as these asperities are of different sizes and shapes, the effect of size on friction/adhesion can be studied using different radii tips. Bhushan and his co-workers[4–11] have used these instruments to study various tribological phenomena such as surface roughness, adhesion, friction, scratching, wear, detection of material transition etc. For example, Ruan and Bhushan[4] used FFM to study a freshly cleaved highly-oriented pyrolytic graphite surface and found that the atomic-scale friction and the topography exhibited the same periodicity but the peaks were displaced relative to each other, which was explained by the variation in interatomic force in the normal and lateral directions. Bhushan and Ruan[11] studied the mechanism of material removal with an AFM. Recently, Bhushan[12] presented a comprehensive review of AFM/FFM studies on the siginificant aspects of nanotribology, nanomechanics and material characterization.

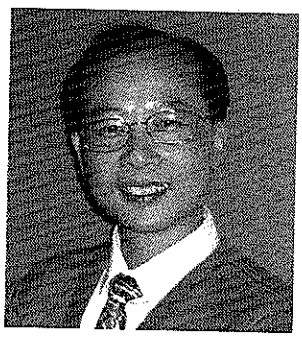

Liangchi Zhang is a professor at the University of Sydney, Australia. He received his Bachelor of Science in 1982 and Master of Engineering in 1985 from Zhejiang University China, then his Doctor of Philosophy in 1988 from Peking University China, all in solid mechanics. From 1989 to 1991, he worked as a post-doctoral research assistant at the University of Cambridge, UK, on elastic-plastic contact mechanics. After that, he worked in Japan shortly as an STA research fellow in the area of grinding at the then Mechanical Engineering Laboratory in Tsukuba. He joined the University of Sydney in 1992 and since then has been working in the areas of nanomechanics and nanomaterials, tribology, solid mechanics, and precision machining. In 2005, he was awarded a Doctor of Engineering by the University of Sydney for his research achievement in *Modeling and Characterisation of Materials and Systems for Precision Manufacturing*. He is an author or co-author of 3 books and over 150 journal papers, an editor or co-editor of 6 books, and a co-inventor of 2 patented technologies of grinding. More details of his research activities can be found at http://nt-542.aeromech.usyd.edu.au/

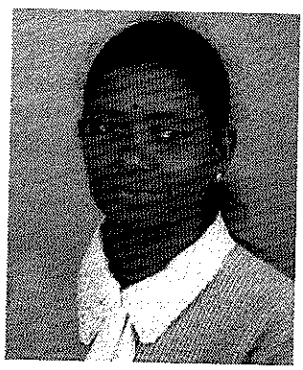

Dr. Kausala Mylvaganam is a research fellow at the University of Sydney, School of Aerospace, Mechanical and Mechatronic Engineering. She received her B.Sc. First Class Honours in Science, specialising in chemistry from the University of Jaffna, Sri Lanka. Thereafter, she received her Ph.D. in chemistry from the University of Cambridge, UK for her work on the *ab initio* calculation of molecular properties, within the field of computational and theoretical chemistry. After achieving her doctorate, she worked as a Senior Lecturer in the Department of Chemistry, University of Jaffna, SriLanka and later as a Research Fellow in chemistry at the University of Cambridge, UK, the University of Sydney and the University of New South Wales, where she worked on several research projects involving quantum mechanics and molecular dynamics. Currently she is doing research in nanotechnology with a particular focus on the modelling of ultra-precision machining and characterization of materials. She is also involved in the computational modelling of carbon nanotubes and its composites.

The advent of super computers for large scale atomic simulations have led to the development of computational micro- and nano-tribology. While quantum mechanics is ideal for very small models on the atomic scale and micro/continuum mechanics is powerful for analysing the objects of micro and macroscopic dimensions, molecular dynamics simulation provides useful means for detailed characterisation of materials on the nanometer scale. The advantage of using molecular dynamics lies in its capacity in handling relatively large molecular systems, which is hard for quantum mechanics to tackle, and its reliability in exploring atomistic deformation mechanisms such as phase transformations and dislocation emitions, to which micromechanics and continuum mechanics are not applicable. Thus, simulations provide useful insight into experimental observations that may lead to the discovery of new phenomena or act as drivers for new experiments that in-turn may lead to an eventual solution to the engineering problems in trobology. Moreover, 3D-computer visualization and animation allow us to follow the atomistic behaviour at different time steps that helps to understand the chemistry and mechanics of the processes.

Fundamentally, a molecular dynamics analysis involves calculating the phase-space trajectories of each atom based on its interaction with other atoms in accordance with Newtonian dynamics. The phase space trajectory describes the motion of an atom by describing its position in the Cartesian coordinate and its momentum. Although the principle of molecular dynamics is simple, a reliable application of the technique requires sophisticated considerations on the details of every step in the modelling and simulation.

This review will elaborate on some fundamental concepts and features of molecular dynamics modelling for characterising the nanodeformation mechanisms of advanced materials, with some analysis of diamond-copper and diamond-silicon sliding system as the examples.

2. MOLECULAR DYNAMICS MODELLING OF MATERIALS

2.1. Initial Model

The very first step in the nanodeformation characterization of a material subjected to a nano-processing operation using the molecular dynamics analysis is to generate an initial molecular model of the material consistent with the operation. Here the nano-processing operation can be any process corresponding to external loading, either simple or complex, such as tension, bending, indentation, tribological sliding and mechanical cutting. One way to generate the initial model[13] is to locate atoms on a perfect lattice structure of a material that represents the real atomic structure of the material.[†] For example, atoms in a model to simulate copper will be positioned in accordance to a face centred cubic (FCC) lattice structure with its lattice constant,[14] while a model to simulate diamond will be positioned in accordance to a diamond cubic structure.[15]

The model having atoms positioned in such a way implies that additional potential energy between atoms has been artificially applied to the system, because in a real material, atoms are actually vibrating around their equilibrium positions. Before simulation can go on, therefore, it is necessary to 'relax' this constructed initial model from its artificially assigned conditions to its natural equilibrium status consistent with the environmental temperature. This involves the execution of the constant temperature molecular dynamics program for a specified number of time steps with a chosen potential function. During the relaxation process, the velocities of Newtonian and thermostat atoms that are initially assigned based on a normal distribution will gradually reach equilibrium at the specified environmental temperature of the simulation by a velocity scaling. The number of time steps required to run for such a relaxation is determined by the time needed for the model to arrive at this equilibrium temperature specified. Depending on the specific materials and their atomic lattice structures, essential relaxation time steps vary. The details will be discussed in specific examples later in the paper.

2.2. Control of Simulation Temperature

The portion of the material simulated by the molecular dynamics model, often called the control volume, is only a small part of the material in the neighborhood of the deformation zone of interest. This portion in reality is part of the rest of the material or the surrounding environment. As such, any heat generated during a nano-processing within the control volume will be conducted away. If this heat conduction process cannot be simulated in a molecular dynamics analysis, the simulation results can be incorrect. To achieve a reasonable heat conduction outward the control volume, special layers of atoms, called thermostat atoms, must normally be arranged to surround the model, as illustrated in Figure 1, the control volume for a nano-indentation setup. Then based on the temperature conversion rule to be discussed later in this paper, temperature regulation is made so that the temperature due to the kinetic energy of these atoms will always be consistent with the environmental temperature. When the dimension of the control volume is sufficiently large, the arrangement of the thermostat atoms provides an efficient and reliable way for the natural heat conduction in the solid.

The scaling of velocities[14] can be done by

$$V_{new} = V_{old}\sqrt{\frac{\text{Kinetic energy corresponding to the environmental temperature}}{\text{Kinetic energy of a thermostat atom before scalng}}} \quad (1)$$

[†]An alternative is to take the initial positions of atoms from the end of an earlier simulation. However this may not be viable as one may often change the size and shape of a model.

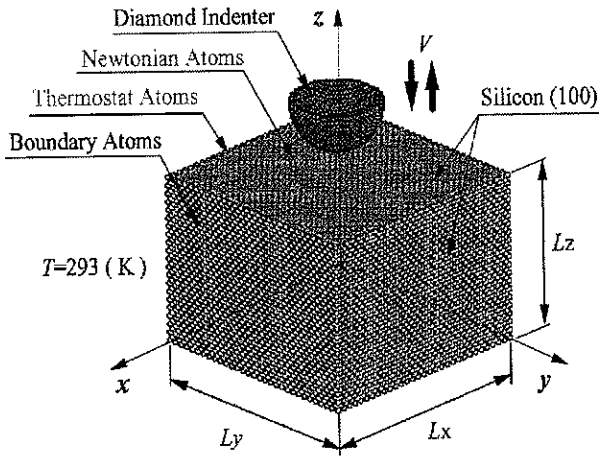

Fig. 1. Molecular dynamics model of silicon specimen with a hemispherical indenter. Reprinted with permission from [15], L. C. Zhang and H. Tanaka, *JSME Int. J. Series A* 42, 546 (**1999**). © 1999, JSME.

where V_{new} is the scaled velocity of a thermostat atom and V_{old} is its original velocity.

2.3. Control Volume

There are three major issues that must be considered in the dimension selection of a control volume of interest. To reduce computational cost, the volume should be as small as possible. However, a too small volume will bring about significant boundary effects that make the results unreliable. These include the boundary temperature effect and the boundary displacement effect. To eliminate these effects, the dimension of the control volume must be sufficiently large so that the temperature at the boundary of the control volume is close to the environmental temperature. Then the application of thermostat atoms can make the natural heat conduction happen in simulation. Similarly, the volume should also be sufficiently large so that the motion of the boundary atoms does not affect the atoms in the deformation zone of interest. Normally, an error analysis is necessary to generate a suitable dimension. Two examples of the selection process of the control volumes for nano-indentation,[15] which has fixed boundary atoms, and those for nano-tribological sliding and nano-machining (nano-cutting, nano-polishing and nano-grinding), which uses moving boundary atoms,[14,16,17] will be discussed in detail later.

2.4. Integration Time Steps

The prediction of the phase-space trajectories of atoms in molecular dynamics simulation is based on the second law of motion of Newton. To solve the differential equation, the finite difference method is often necessary because collisions between atoms are not instantaneous; rather, they are strong repulsive and attractive interactions that occur over a finite duration. However, the use of the

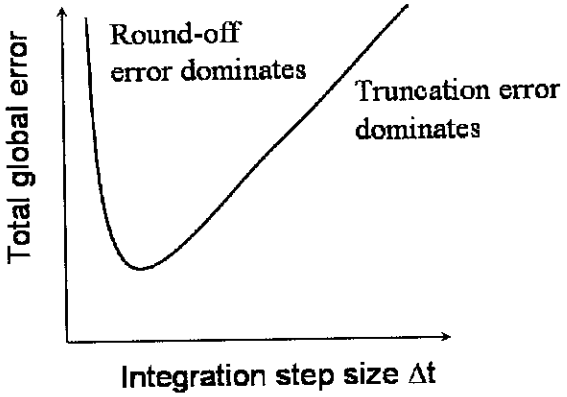

Fig. 2. Different types of errors against the size of time steps. Reprinted with permission from [15], L. C. Zhang and H. Tanaka, *JSME Int. J. Series A* 42, 546 (**1999**). © 1999, JSME.

finite difference method implies that the size of the integration time step, Δt, must be determined very carefully, because both the global truncation error and global round-off error depend on Δt. Moreover, these two types of errors are affected differently by changes in Δt, as shown in Figure 2.[17] The global truncation error decreases with decreasing Δt, while the other depends on the number of calculations. This means that the smaller the size of the time steps, the more calculations to be done and the greater will be the global round-off error.

A way to reduce the round-off error is to have an efficient code and use high precision arithmetic. To reduce the truncation error, however, it is necessary to reduce the size of Δt. It must also be noted that a smaller time step is usually associated with a greater computational cost.

In addition to the above problems, it is essential to note that the finite difference algorithm commonly used in molecular dynamics, the Verlet's method,[13–17] is conditionally stable. That is to say, it will become unstable when Δt reaches a critical value, though the threshold can be determined through a series of experiments. Generally, a suitable time step is recommended to be from 1/28 to 1/32 of the vibration period of an atom.[15,17] Hence the optimum time step is dependent on both the specific material and the potential function used. For instance, with the Tersoff potential,[18,19] an individual atom of silicon or diamond can be forced to move in a direction to determine the corresponding stiffness k, as shown in Figure 3, so that the period of vibration of the atom in the direction, T, can be determined by $T = 2\pi(m/k)^{1/2}$, where m is the mass of the atom.[15,17]

2.5. Temperature Conversion

Another important factor in a successful molecular dynamics analysis is the reliable conversion between the kinetic energy and temperature of an atom. An inappropriate conversion will result in an error in the velocities of the atoms and hence render the simulation incorrect. It is always essential that for a given material, a temperature

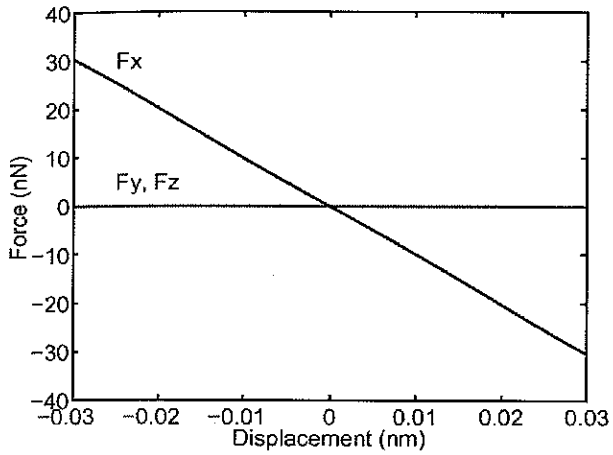

Fig. 3. Force-displacement relationship (Tersoff potential) when moving a silicon atom in the [100] direction. The material stiffness k can be obtained from the gradient of the plot. Reprinted with permission from [15], L. C. Zhang and H. Tanaka, *JSME Int. J. Series A* 42, 546 (**1999**). © 1999, JSME.

conversion model is identified carefully before carrying out a molecular dynamics simulation. In studying the deformation mechanisms of monocrystalline silicon under the nano-indentation and nano-scratching with diamond tools,[15, 16, 20] for instance, there are three models available[21] for the conversion. They are Dulong-Petit's model, which takes into account the independent lattice vibration, Einstein's model, which is based on the consideration of the single characteristic frequency, and Debye's model, which involves a range of frequencies. A comparison with the experimental measurement, as shown in Figure 4, shows that in the temperature regime encountered in the nano-indentation and nano-scratching, the Debye's model is the best for silicon and the Einstein's model is the most suitable for diamond. Clearly, if these models are incorrectly used, the result of molecular dynamics simulation cannot be correct.

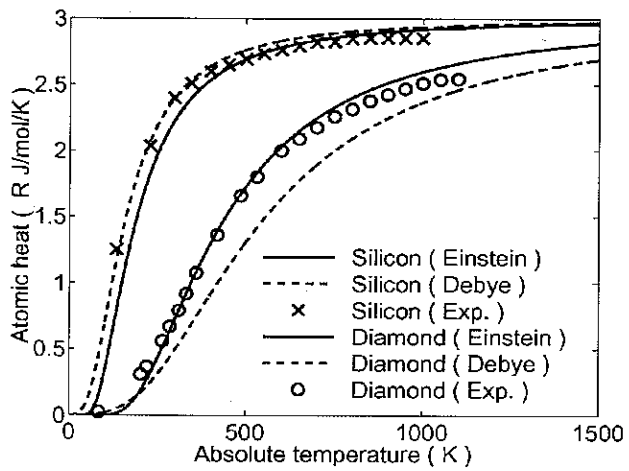

Fig. 4. Comparison of temperature conversion models. Reprinted with permission from [15], L. C. Zhang and H. Tanaka, *JSME Int. J. Series A* 42, 546 (**1999**). © 1999, JSME.

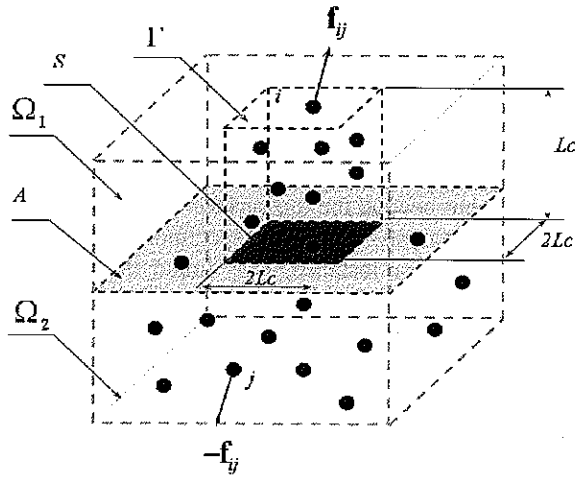

Fig. 5. Concept of stress vector on an atomic scale. Reprinted with permission from [15], L. C. Zhang and H. Tanaka, *JSME Int. J. Series A* 42, 546 (**1999**). © 1999, JSME.

2.6. Stress Analysis

The analysis of stress in a material is an important part in our understanding of characteristics such as deformation or transformation of the material under various machining processes. Stress analysis also allows useful criteria to be set for the prediction of phase transformation or plastic deformation of the material under processing.

However, on a fine scale, materials cannot be treated as a continuum and the conventional definition of stress is no longer valid.[15, 20, 22] Here, let us take the deformation of monocrystalline silicon as an example to introduce the concept of stress analysis on the atomic scale.

Figure 5 shows a conceptual atomistic model for calculating stresses. Assume that a solid is divided into an upper part Ω_1 and a lower part Ω_2 by a plane A. Consider a small element Γ in Ω_1 with a base area S in plane A. The stress on S is defined by

$$\sigma = \frac{\mathbf{F}}{S} \tag{2}$$

where $\mathbf{F}$ is the resultant force on S induced by the interaction between the atoms in Ω_2 and those in Γ and should be calculated by

$$F = \sum_{i=1}^{N_A}\sum_{j=1}^{N_B} f_{ij} - \sum_{i=1}^{N_A}\sum_{j=1}^{N_B} f_{0ij} \tag{3}$$

in which N_A is the number of atoms in Γ, N_B is the number of atoms in Ω_2, f_{ij} is the inter-atomic force vector during indentation between atom i in Γ and atom j in Ω_2 and f_{0ij} is the inter-atomic force vector before indentation between atom i in Γ and atom j in Ω_2. The contribution of interatomic forces before indentation, f_{0ij}, must be eliminated as the stress analysis considers only the effect of deformation due to external forces. This consideration ensures consistency with the definition of stress in continuum mechanics.

It is important to note that in continuum mechanics a stress vector is defined at a mathematical point but in the definition here on the atomic scale, area S should always be finite. Moreover, to obtain a representative stress vector on S, the height of the element must be selected in a way that the interaction force between atom j in Ω_2 and atom i in Ω_1 but beyond the top surface of Γ is negligible. In the stress analysis of silicon specimen subjected to nano-indentation, for instance, it is found that the optimum size for element Γ is $2L_c \times 2L_c \times 2L_c$ as shown in Figure 5, where $L_c = 0.543$ nm is the side length of a unit cell of silicon.

There are two questions that arose from the above stress definition on a molecular scale. The first pertains to the momentum flux of atoms within the material. That is if it is necessary to consider the contribution of this element in the calculation of stresses. In fact, each element of the stress tensor will compose of a kinetic part and a potential part, i.e.,

$$J_{\alpha\beta} = m\sum_{i}^{N} v_{i\alpha}v_{i\beta} + \frac{1}{2}\sum_{i\neq j}^{N} r_{ij\beta}F_{ij\alpha} \tag{4}$$

where m is the atomic mass, $v_{i\alpha}$ is the α-component of the velocity of atom i, $r_{ij\beta}$ is the β-component of the vector $\mathbf{r}_{ij}$ separating atoms i and j, and $F_{ij\alpha}$ is the α-component of the force exerted on atom i by atom j. However, simulation results have shown that for a solid, the contribution due to the momentum flux of atoms within the body is very small compared to the effects of inter atomic forces between the atoms. Hence, if the simulation is done for a solid, this term can be neglected.

The second question is that when a material is under an external load applied by another solid, e.g., in the case of nano-indentation involving both the workpiece material (monocrystalline silicon) and the tool (diamond indenter), if it is necessary to include the interaction forces between the workpiece and tool atoms in the stress analysis of the workpiece. It has been shown that the effect of this interaction is small when the work-tool interactive potential is low and hence is negligible if the region of interest for the stress analysis is not in close proximity with the tool. Stress calculation of the workpiece in such cases can therefore be achieved by considering the atoms of the workpiece alone. However, if the work-tool interactive potential is high, the influence of the tool atoms must be considered.

2.7. Potential Function

Given the adequacy of the simulation techniques and the appropriate selection of the control volume and time step size, the reliability of the results of a simulation depends on the quality of the atomic interaction potential used. If the potential function does not model the behavior of the atoms correctly, the results produced will be unable to simulate the actual deformation correctly.

It would be desirable to take the interactions directly from first principle calculations. However, this would take up far too much computational time. Thus in orders to obtain useful atomic interactions, empirical potentials have been developed.

In general the potential energy of a system of N atoms is a function of the atomic co-ordinates. Thus the potential energy may be expressed in a series of n-body inter-atomic potentials

$$\phi_{\text{total}} = \phi_o + \Sigma\phi_1(i) + \Sigma\phi_2(ij) + \Sigma\phi_3(ijk) + \cdots + \phi_N(ijkl,\ldots) \tag{5}$$

where ϕ_n is the n-body interaction potential which is a function of the positions of n atoms $ijk\ldots$ The sums in Eq. (5) are over all combinations (excluding redundant contributions) of n atoms in the system. The potential ϕ_n, and the number of terms, which are retained in a practical application, depends on the nature of the system under investigation.

In s-p bonded metals, i.e., metals with free electrons outside the ion cores, the structure-dependent part of the system energy can be accurately expressed in terms of the second-order (pair potential) terms of Eq. (5). Hence pair potentials (such as Lennard-Jones, Morse, etc.) have a firm theoretical basis in simple metals.[23] Examples of such metals are copper, sodium, magnesium, and aluminium. Zhang and co-workers have employed the Morse pair potential in the modeling of copper atoms and find the results of the simulation satisfactory.[14,24] A detailed explanation and expression for the Morse potential used in the modeling of copper can be found in Ref. [14].

When using the pair potential function, the omission of angle dependent forces and many-body effects results in a severe restriction on its application to more covalent systems such as silicon where the directionality of the localization of charge in the bonding region is important. In such cases, it will require an empirical potential incorporating two and three-body interactions. The parameters used in the potential function can be determined by least-square fits to a database of calculated energies of real and hypothetical atomic structures. However, due to the exclusion of some atomic structures, it is often difficult to evaluate the generality of such potential. Also, this method of simulation requires much computational time.

To address these shortcomings of the above-mentioned potential function, the Tersoff potential was developed. This replaces the traditional two and three-body expansion of the interaction energy with a simple pair-like potential where the bond order of the atoms is affected by its local environment.[18,19] In this way, structural chemistry is included in a classical empirical potential. It has been found that energies and geometries for silicon are very well described using the Tersoff potential. A detailed explanation and expression for the Tersoff potential is given below.

The total Tersoff energy E_T, is modeled as a sum of pair like interactions and can be expressed as,

$$E_T = \sum_i E_i = \frac{1}{2}\sum_{i \neq j} W_{ij} \tag{6}$$

where W_{ij} is the bond energy so that the summation in the equation is about all the atomic bonds in the control volume. W_{ij} is a function of repulsive pair potential f_R, and attractive pair potential f_A, and has the form of

$$W_{ij} = f_C(r_{ij})[f_R(r_{ij}) + b_{ij} f_A(r_{ij})] \tag{7}$$

where

$$f_R(r_{ij}) = A_{ij}\exp(-\lambda_{ij} r_{ij}), \quad f_A(r_{ij}) = B_{ij}\exp(-\mu_{ij} r_{ij})$$

$$f_C(r_{ij}) = \begin{cases} 1 & r_{ij} \leq R_{ij} \\ \frac{1}{2} + \frac{1}{2}\cos\pi(r_{ij} - R_{ij})/(S_{ij} - R_{ij})], & R_{ij} \leq r_{ij} \leq S_{ij} \\ 0 & r_{ij} \geq R_{ij} \end{cases}$$

$$b_{ij} = \chi_{ij}(1 + \beta_i^{n_i}\zeta_{ij}^{n_i})^{-1/2n_i}$$

$$\zeta_{ij} = \sum_{k \neq i,\, j} f_C(r_{ij}) g(\theta_{ijk})$$

$$g(\theta_{ijk}) = 1 + c_i^2/d_i^2 - c_i^2/[d_i^2 + (h_i - \cos\theta_{ijk})^2]$$

$$\lambda_{ij} = (\lambda_i + \lambda_j)/2, \quad \mu_{ij} = (\mu_i + \mu_j)/2$$

$$A_{ij} = (A_i A_j)^{1/2}, \quad B_{ij} = (B_i B_j)^{1/2}$$

$$R_{ij} = (R_i R_j)^{1/2}, \quad S_{ij} = (S_i S_j)^{1/2} \tag{8}$$

Here, i, j, and k label the atoms, r_{ij} is the length of the ij bond and θ_{ijk} is the bond angle between bonds ij and ik. Other parameters such as A, B, R, S, λ, χ, and μ, as listed in Table I, are Tersoff potential parameters, depending on individual materials. With Eqs. (6) and (7), the interaction forces between silicon atoms can be obtained by calculating the gradient of E_T.

The interaction between the silicon and diamond indenter atoms is modelled by the modified Morse potential[14] given by

$$\phi(r_{ij}) = \lambda_1 D[e^{-2\lambda_2\alpha(r_{ij} - r_0)} - 2e^{\lambda_2\alpha(r_{ij} - r_0)}] \tag{9}$$

Table I. Parameters in Tersoff potential for carbon and silicon.

	Carbon	Silicon
A (eV)	1.3936×10^3	1.8308×10^3
B (eV)	3.4670×10^2	4.7118×10^2
$\lambda\mu$	34.879	24.799
μ	22.119	17.322
β	1.5724×10^{-7}	1.1000×10^{-6}
n	7.2751×10^{-1}	7.8734×10^{-1}
c	3.8049×10^4	1.0039×10^5
d	4.384×10^0	1.6217×10^1
h	-5.7058×10^{-1}	-5.9825×10^{-1}
R (nm)	0.18	0.27
S (nm)	0.21	0.30
$\chi_{C-C} = 1.0$	$\chi_{Si-Si} = 1.0$	$\chi_{C-Si} = 0.9776$

Table II. Parameters in the standard Morse potential.

Parameter	C–Si
D (eV)	0.435
α (nm^{-1})	46.487
r_o (nm)	0.19475
λ_1	1
λ_2	1

The parameters such as D, α, r_o are shown in Table II. Interaction force is calculated by the gradient of ϕ.

3. NANO-TRIBOLOGY

3.1. Introduction

A full understanding of friction and wear on the atomic scale is of fundamental importance to the development of nanotechnology. Immediate examples in which atomic friction and wear play a central role are the optimal design, fabrication and operation of devices with atomic resolution, such as micro-machines and high-density magnetic recording systems. Over the last two decades or so, many studies have been carried out to explore the mechanisms of nano-friction and nano-wear, both theoretically and experimentaly. For instance, an early experimental observation of atomic scale friction using an atomic force microscope was reported by a research group at IBM.[25] The friction coefficient between a tungsten tip of radius 300 nm and a basal plane of a graphite grain was found to be 0.012 at a normal load of 10 μN. Another early interesting study[26] was about the sliding of a tungsten tip of radius 10 μm on a carbon sputtered surface. A frictional force of about 1 μN at zero normal force was measured, indicating an infinite friction coefficient. In the meantime, theoretical studies using molecular dynamics simulation and the first-principle calculations[27–31] have also been carried out and showed that friction coefficient could vary significantly, from 0.01 to 0.07, under different sliding conditions. Recently, the work reported by Mulliah et al.[32] on the indentation and scratching of Ag(100) surface by a pyramidal diamond indentor, showed that the shape of the tip affects the friction coefficient and it is dependent on both the orientation of the indentor and the indentation depth. Belak and Stowers[33] studied the indentation and scraping of a copper monocrystal by a rigid diamond tip using the molecular dynamics simulation. While focusing mainly on some issues of indentation with an observation of dislocation initiation, they also simulated a cutting under a specific condition and observed that the friction coefficient was about 1.0. However, the mechanisms of friction and wear and the effect of deformation, sliding conditions and dislocation motions were not studied.

A more systematic research was conducted by Homola,[34] who proposed the concept of interfacial sliding

REVIEW

to describe the sliding of two perfect, molecularly smooth and undamaged mica surfaces. Mechanisms of wear also addressed. The investigation demonstrated that the Bowden-Tabor formula,[35] which states that the frictional force is proportional to the real molecular contact area, could well describe the frictional behaviour during atomic sliding. In fact, the importance of the atomic contact area to atomic friction is not difficult to understand if the JKR theory[36, 37] is recalled. This theory, while considering the effect of surface energy in its analysis, has implicitly indicated that the real contact area must be of great concern to sliding loads on the atomic scale.

If looking into the details of contact sliding, we can have two primary situations. When two surfaces are in sliding without foreign particles, they are in two-body contact sliding, as shown in Figure 6(a). In this case, the interactions among surface asperities play a central role in the process of wear and friction. However, if some particles appear between the surfaces, which could be the debris from worn surfaces or foreign particles due to contamination, a three-body contact sliding occurs, as shown in Figure 6(b). Under such circumstances, the kinetics and properties of the particles contribute to the tribology of the surfaces. The above sliding processes are common in nanotribological systems.

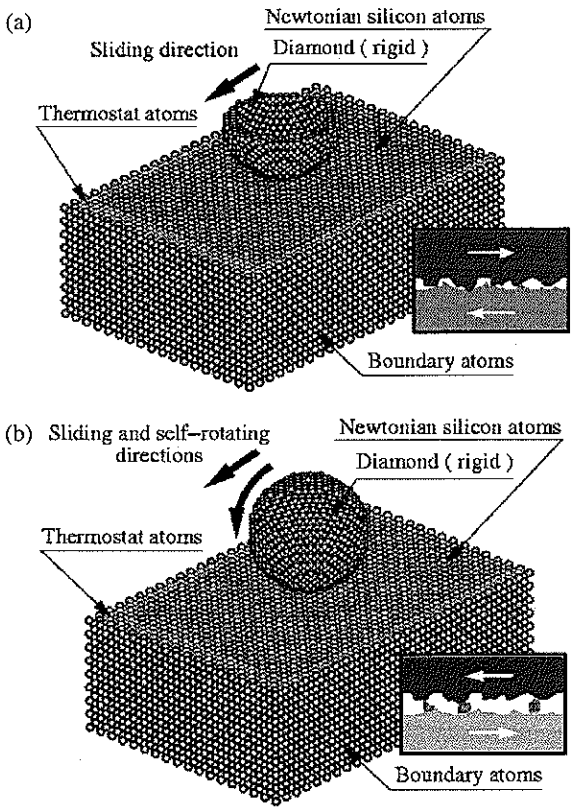

Fig. 6. Molecular dynamics modeling of the sliding processes. (a) two-body sliding and (b) three-body sliding. Reprinted with permission from [16], L. C. Zhang and H. Tanaka, *Tribol. Int.* 31, 425 **(1998)**. © 1998, Elsevier Science.

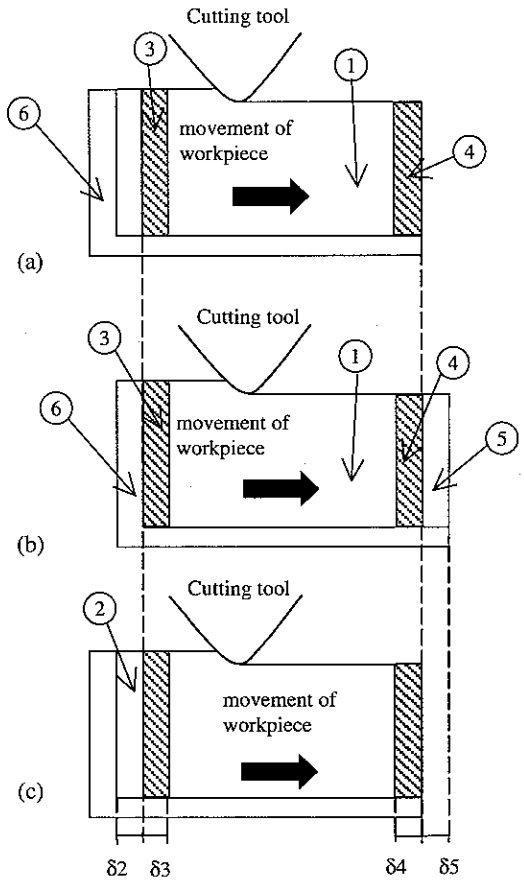

Fig. 7. The concept of moving control volume of a workpiece subject to nano-cutting. (a) Initial control volume, (b) The control volume before the operation of removal and addition, and (c) The control volume after the operation of removal and addition. Reprinted with permission from [38], W. C. D. Cheong et al., *Key Engineering Materials* 196, 31 **(2001)**. © 2001, Trans Tech Publications.

3.2. Moving Control Volume

To simulate a sliding or cutting process, the distance of relative motion of an asperity to a workpiece is significant.[‡] An apparent way of simulating the steady-state behaviour of the workpiece material is to take a large portion of the work material as the control volume for simulation. However, this is infeasible because the cost and capacity of computation limit the number of atoms in a model. The moving control volume technique[14, 16, 17, 38] is then necessary and advantageous, in which the dimension of the control volume is similar to that of a non-moving one but with special atom removal and addition techniques. Shown in Figure 7 is an example of using the moving control technique for simulating nano-cutting, where Zone 1, the zone affected by cutting deformation, is equivalent to the normal control volume size discussed previously. Zones 2 to 5 are those unaffected by the cutting deformation. When the cutting proceeds, atoms in Zone 5 can be removed because

[‡]In grinding and polishing, the situation is similar.

the removal will not affect the behaviour of the atoms in Zone 1. However, Zone 4 becomes a transition one because the boundary between Zones 4 and 5, which is originally inside the workpiece, becomes a free surface. The dimensions of both $\delta 4$ and $\delta 5$ must be determined by an error analysis such that the removal of Zone 5 and the creation of the new free surface do not influence the behaviour of atoms in Zone 1. Similarly, because atoms are added in Zone 2 after the removal of atoms from Zone 5, Zone 3 becomes a transition zone. Owing to the same reason, the dimensions of both $\delta 2$ and $\delta 3$ must also be determined by an error analysis. Zone 6 consists of the boundary and thermostat atoms.

3.3. Diamond-Copper Sliding Systems

3.3.1. Methods of Modelling and Analysis

For simplicity, let us consider an atomically smooth diamond asperity sliding on an atomically smooth surface of a copper monocrystal in its (1 1 1) plane. The variables of interest are the sliding speed V, indentation depth d, degree of surface lubrication or contamination and the tip radius of asperity R that is the radius of the envelope of centres of the surface atoms. The environmental temperature of the sliding system is 293 K and the asperity rake angle is $-60°$. In addition, we assume that d keeps constant in a sliding process, which implies that the sliding system has an infinite loop stiffness.

The interactions between copper atoms can be described by the modified Morse potential given in Eq. (9), where r_{ij} is the interatomic separation between atoms i and j, r_0 is the equilibrium separation at which the potential minimises. D and α are material constants listed in Table III. The physical meaning of D is the cohesive energy between the two atoms. λ_1 and λ_2 are non-dimensional parameters indicating the cohesive strength change between the atom pair $i-j$. For copper-copper atom pairs, $\lambda_1 = \lambda_2 = 1$, hence Eq. (9) becomes identical to the standard Morse potential. For copper-diamond atom pairs, however, λ_1 takes a value in interval (0, 1] whilst $\lambda_2 \geq 1$. This is because an application of lubrication or contamination on the diamond-copper interface weakens the cohesive strength between copper and diamond atoms. Hence the effect of surface lubrication or contamination on the friction and wear can be qualitatively investigated by varying λ_1 in (0, 1] and ignoring the detailed effects of lubricant or contaminant atoms. However, when λ_1 varies in (0, 1], the potential curve between a pair of copper-diamond atoms will distort towards the negative direction of r. Bearing in mind that the atomic distance between any copper and diamond atoms increases, rather than decreases, when a lubricant or contaminant atom appears to separate them from direct contact, the potential curve should distort towards the positive direction of r. Hence λ_2 in Eq. (9) must be larger than one. In the present analysis, we determine λ_2, when λ_1 changes, by keeping the spring constant of a copper-diamond atomic pair unchanged.[#]

Table III. Parameters in the standard Morse potential.

Parameter	Cu–Cu	Cu–C
D (eV)	0.342	0.087
α (nm^{-1})	13.59	51.40
r_0	0.287	0.205

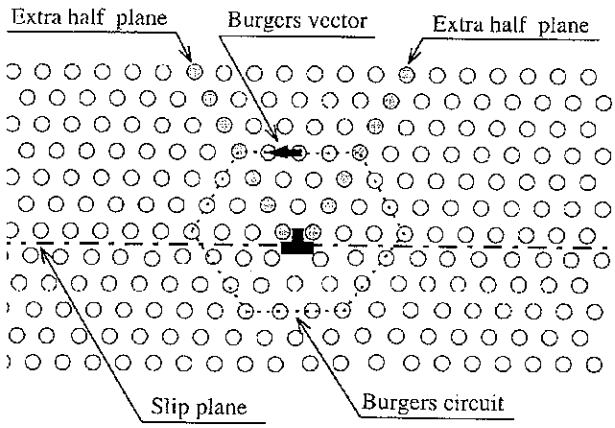

Fig. 8. Determination of edge dislocations. Reprinted with permission from [14], L. C. Zhang and H. Tanaka, *Wear* 211, 44 **(1997)**. © 1997, Elsevier Science.

With the above potential function available, the forces on atom i due to the interaction of all the other atoms can be calculated by

$$F_i = -\sum_{j=1, j\neq i}^{N} \Delta_i \phi(r_{ij}) \tag{10}$$

where N is the total number of atoms in the model,[$] including thermostat, boundary and diamond atoms. Consequently, the motion of all the Newtonian atoms in the control volume, including their instant position and velocity vectors, can be obtained by following the standard procedures of molecular dynamics analysis described previously.

In principle, an asperity is three-dimensional and thus a three-dimensional molecular dynamics analysis would be more appropriate. However, we found, based on a careful comparison,[39] that a two-dimensional model can lead to accurate enough results in terms of the variations of temperature and sliding forces and easier characterisation of deformation. We will therefore focus on the two-dimensional, plane-strain analysis in this section.

When an instant configuration of the copper atomic lattice during sliding is obtained by the molecular dynamics analysis, the distribution of dislocations in the deformed lattice can be determined by the standard dislocation analysis.[40] Figure 8 shows an example of identifying edge

[#]This means that when λ_1 is given, λ_2 is determined by $(\lambda_1 D)(\lambda_2 \alpha)^2 = D\alpha^2$; hence $\lambda_2 = \lambda_1^{-1/2}$.

[$]Here, $12{,}000 \leq N \leq 15{,}000$ is used in conjunction with the technique of moving control volume.

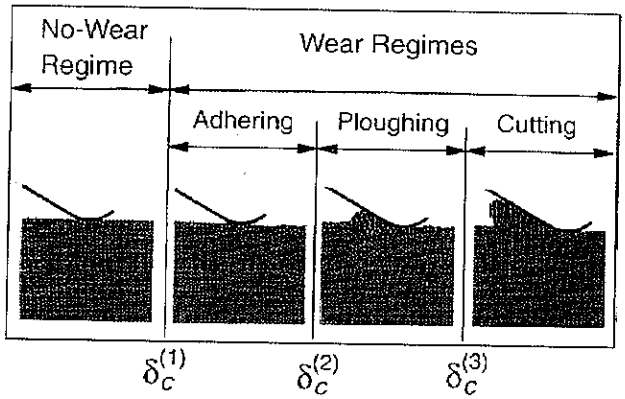

Fig. 9. The transition diagram of deformation regimes. (The diamond slides from the right to the left). Reprinted with permission from [14], L. C. Zhang and H. Tanaka, *Wear* 211, 44 (**1997**). © 1997, Elsevier Science.

dislocations when two extra half planes of atoms (dark atoms) appear in the deformed atomic lattice. The Burgers vector can be obtained by application of the Burgers circuit. Since we are now carrying out a two-dimensional molecular dynamics simulation, we can only study edge dislocations.[39] For convenience, however, we call them dislocations thereafter.

3.3.2. *Mechanisms of Wear*

The deformation of the copper specimen has four distinct regimes under sliding. They are the *no-wear regime*, *adhering regime*, *ploughing regime*, and *cutting regime*, as shown in Figure 9. In the figure, the transition of deformation regimes is characterised by the non-dimensional indentation depth δ, which is defined as d/R and can be viewed, when contact sliding takes place, as a measure of the strain imposed by the diamond asperity.

In the no-wear regime, the atomic lattice of copper is deformed purely elastically. After the diamond asperity slides over, the deformed lattice recovers completely. In this case, sliding does not introduce any wear or initiate any dislocation.

When δ increases and reaches its first critical value, $\delta_c^{(1)}$, adhering occurs. The atomic bonds of some surface copper atoms are broken by the diamond sliding. These copper atoms then adhere to the asperity surface and move together with it. However, they may form new bonds with other surface atoms of copper and return to the atomic lattice. The above process repeats again and again during sliding, causes a structure change of the copper lattice near the surface, and creates surface roughness of the order of one to three atomic dimensions. In the meantime, some dislocations are also activated in the subsurface, see Figure 10(a).

If δ increases further to its second critical value, $\delta_c^{(2)}$, the above adhering deformation will be replaced by ploughing (Fig. 9 and Fig. 10(b)). An apparent feature of deformation

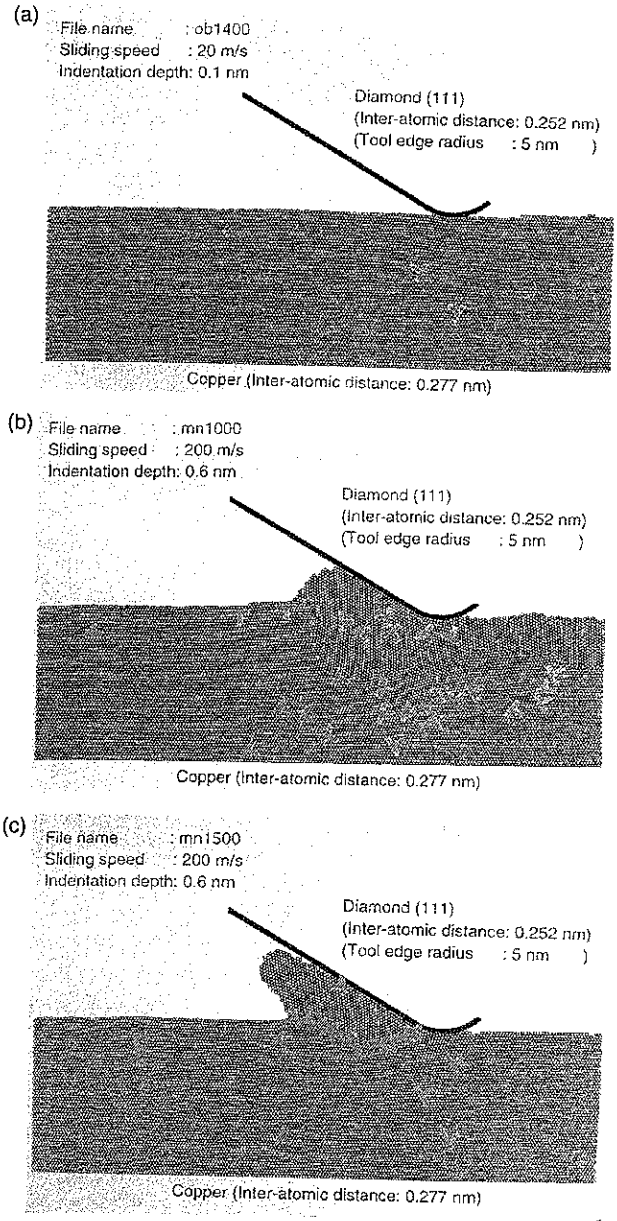

Fig. 10. Distribution of dislocations in the subsurface of copper specimen. (The diamond slides from the right to the left). (a) adhering regime, (b) ploughing regime, and (c) cutting regime. Reprinted with permission from [14], L. C. Zhang and H. Tanaka, *Wear* 211, 44 (**1997**). © 1997, Elsevier Science.

in the stage is that a triangular atom-cluster always exists in front of the leading edge of the diamond asperity and appears as a triangular wave being pushed forward. In this regime, the deformation zone in the subsurface becomes very large and a great number of dislocations are activated. Moreover, the motion of dislocations and their interactions in the subsurface become extremely complex. Grain boundaries can also be generated by ploughing, as shown, for instance, by the continuous orange curve in Figure 10(b).

When δ reaches its third critical value, $\delta_c^{(3)}$, a new deformation state, cutting, appears, characterised by chip

formation. Compared with the ploughing regime, the dimension of the deformation zone during cutting is smaller. Dislocations distribute much more closely to the sliding interface (Fig. 10(c)).

The above figure of deformation regimes and their transition represents the most general case. Under some specific sliding conditions, not all the regimes would appear except the no-wear regime.

For example, if the tip radius of the diamond asperity keeps unchanged but the sliding speed changes, then at lower sliding speeds all the four regimes described above appear. At higher speeds, however, ploughing regime vanishes, see Figure 11(a). On the other hand, at a given sliding speed, if the tip radius of the asperity is very small, say 1 nm, only no-wear and cutting regimes emerge, as shown in Figure 11(b). However, with relatively larger tip radii, adhering appears as a transition from no-wear to cutting.

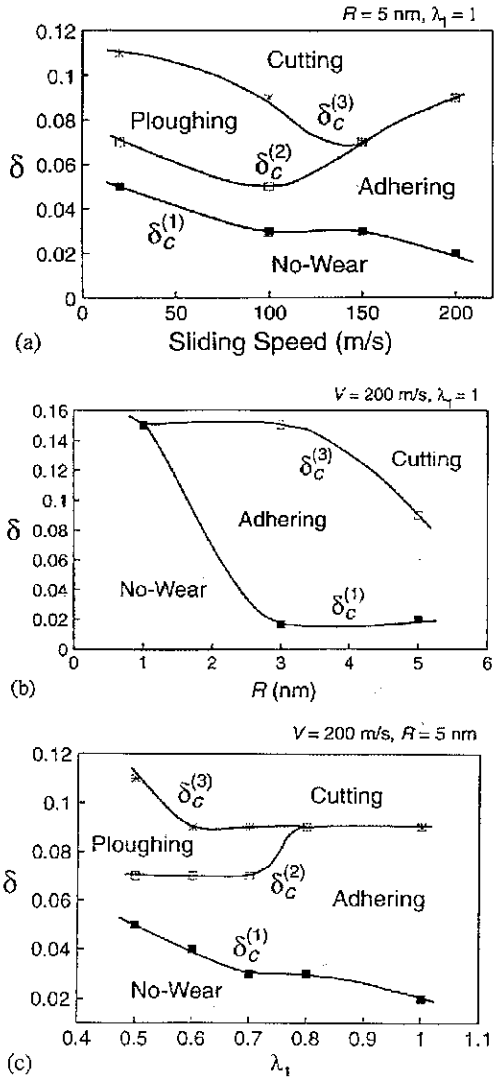

Fig. 11. Regime transition under specific sliding conditions. (a) non-dimensional indentation depth versus sliding speed, (b) non-dimensional indentation depth versus tip radius, and (c) non-dimensional indentation depth versus lubrication/contamination. Reprinted with permission from [14], L. C. Zhang and H. Tanaka, *Wear* 211, 44 (**1997**). © 1997, Elsevier Science.

Another important factor that alters the deformation transition is the effect of surface lubrication or contamination. If the sliding interface is chemically clean, $\lambda_1 = \lambda_2 = 1$ in Eq. (9). In this case, as shown in Figure 11(c), ploughing does not happen at a given sliding speed and tip radius. If the surface is lubricated, $\lambda_1 \leq 1$ with $\lambda_2 \geq 1$, and all the four regimes occur.

It is obvious from Figure 11 that the no-wear regime exists in a wide range of indentation depths. In addition, a smaller radius, a lower sliding speed, or a better surface lubrication (i.e., smaller λ_1) enlarges the no-wear regime. This highly indicates that a no-wear design of sliding systems may be possible in practice. Moreover, it is important to note that the size of the no-wear regime is a strong function of sliding speed and surface lubrication. Therefore, sliding speed and lubrication should be taken into specific account in an attempt to design no-wear sliding systems. Very recently from a carbon-on-copper roller-sliding study, Jeng et al.[41] reported that minimum resistance at the interface depends on the angular velocity of the roller and the separation distance between the roller and the slab. They found that a negative angular velocity minimizes wear and deformation at the interface.

The formation of various deformation regimes and their transition can be elucidated by the variation of temperature distribution and dislocation motion in the atomic lattice, see Figure 10 and Figure 12. For instance, a larger indentation depth or a higher sliding speed indicates a higher input sliding energy, greater temperature rise and severe plastic deformation. This in turn means a higher density of dislocations with more complicated interactions in the deformed atomic lattice. When the non-dimensional indentation depth δ is small, a smaller number of atoms have high temperatures, as shown in Figures 12(a) and 12(b). Sliding does not cause any considerable temperature rise in the vicinity of the contact zone. With the increase of δ, the number of high temperature atoms increases quickly (Figs. 12(c) and 12(d)). However, compared with the cutting regime (Fig. 12(d)), the high temperature atoms in the ploughing regime (Fig. 12(c)) distribute in a much wider area. This explains why a ploughing regime has a greater deformation zone and less localised distribution of dislocations (Fig. 10).

3.3.3. *Friction*

With the above deformation mechanisms in mind, now let us examine the frictional behaviour of the system. Figure 13 shows the variation of the conventional friction coefficient, $\mu = |F_x/F_y|$, with the change of δ, where F_x and F_y are respectively the frictional force and normal indentation force during sliding. It is clear that in the cutting regime, F_x is proportional to F_y. In other

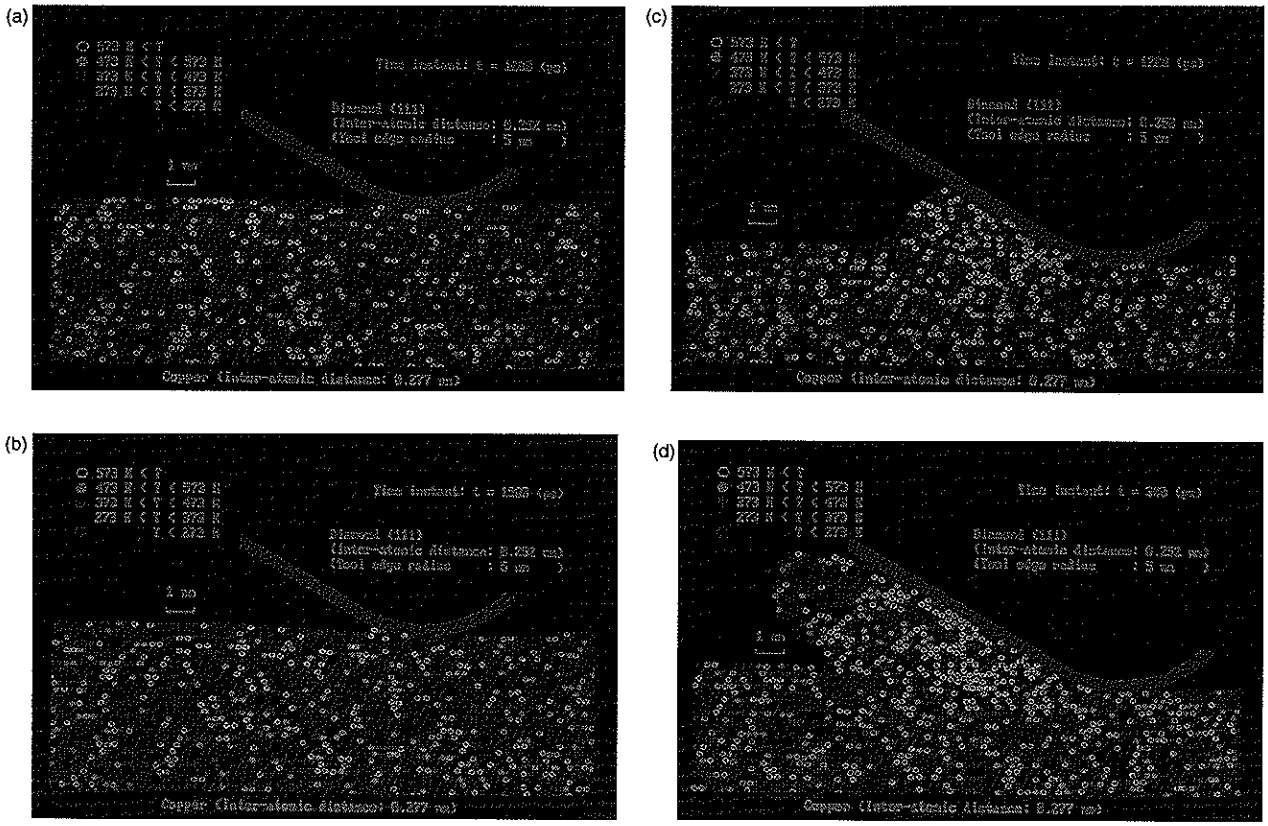

Fig. 12. Temperature distribution in the atomic lattice of copper. (The diamond slides from the right to the left). (a) no-wear regime, (b) adhering regime, (c) ploughing regime, and (d) cutting regime. Reprinted with permission from [14], L. C. Zhang and H. Tanaka, *Wear* 211, 44 **(1997)**. © 1997, Elsevier Science.

regimes, however, the behaviour of F_x is complex. Particularly, μ becomes singular at a specific δ in the no-wear regime.

The singularity of μ is understandable if we examine the sliding forces when δ changes. On the atomic scale, as shown in Figure 14, the normal sliding force F_y always varies from attractive to repulsive. Thus at the transition point ($F_y = 0$), μ is infinite. This also explains why μ varies sharply under different sliding conditions as reported by Refs. [26–32]. All these clearly indicate that the concept of the conventional friction coefficient is no longer meaningful in no-wear, adhering and ploughing regimes.

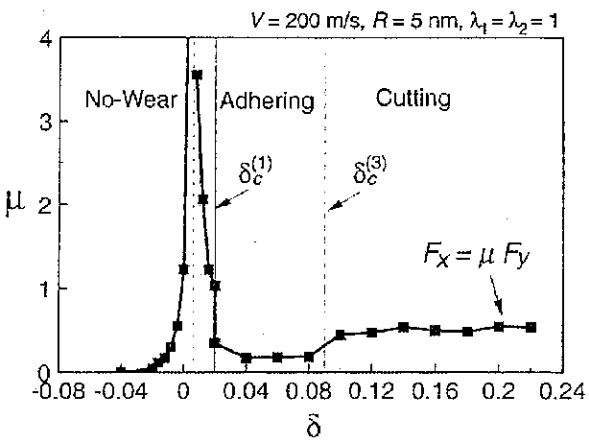

Fig. 13. Variation of friction coefficient. Reprinted with permission from [14], L. C. Zhang and H. Tanaka, *Wear* 211, 44 **(1997)**. © 1997, Elsevier Science.

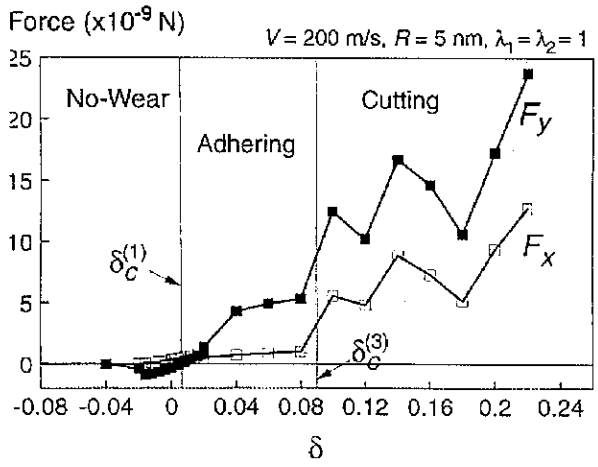

Fig. 14. Variation of sliding forces. Reprinted with permission from [14], L. C. Zhang and H. Tanaka, *Wear* 211, 44 **(1997)**. © 1997, Elsevier Science.

In non-contact sliding, the only appropriate way to calculate the frictional force is to use Eq. (10). In contact sliding, however, empirical expressions in terms of the contact area can be developed. For example, the following simple formula can be obtained according to the present theoretical analysis,

$$F_x = \begin{cases} -\sum_{n=1}^{N_d}\sum_{m=1}^{N_c}\frac{\partial}{\partial x_n}\phi(r_{mn}), & \text{for } L_c = 0 \\ \zeta_1^{II} L_c w_a + \zeta_2^{II}, & \text{for } L_c^{(1)} < L_c \le L_c^{(2)} \\ \zeta_1^{III} L_c w_a + \zeta_2^{III}, & \text{for } L_c > L_c^{(2)} \end{cases} \quad (11)$$

where $\zeta_1^{II} = 409$ MPa, $\zeta_2^{II} = 1.807 \times 10^{-8}$ nN, $\zeta_1^{III} = 4.20$ GPa, $\zeta_2^{III} = -1.899$ nN are constants, N_c is the total number of copper atoms in the model, N_d is the number of diamond atoms, L_c is the atomic contact length and $w_a = 0.226$ nm is the width of an atomic layer of copper in the direction perpendicular to its (1 1 1) plane. Equation (11a) can be derived directly from Eq. (10) by considering that F_x is the resultant force of the atomic forces on all the diamond atoms in x-direction. Eqs. (11b) and (11c) are empirical expressions by fitting the MD simulation data in Figure 15. The physical meaning of product $L_c w_a$ in Eq. (11) is the atomic contact area in the present sliding system. As shown by Eq. (11) and Figure 15, we can see that the frictional behaviour of an atomic sliding system cannot be described by a single formula. There exist two distinct contact sliding zones, Zone II ($L_c^{(1)} \le L_c < L_c^{(2)}$) and Zone III ($L_c \ge L_c^{(2)}$), where $L_c^{(2)} = 2.216$ nm is the transition boundary from Zones II to III, and $L_c^{(1)} = 0.277$ nm is the minimum contact length defined as the distance between two copper atoms in its (1 1 1) plane. The transition from non-contact to contact sliding is a sudden change because L_c does not exist below $L_c^{(1)}$. In Figure 15, Zone II reflects the frictional behaviour of the system in the no-wear contact sliding, while Zone III shows that in the adhering and ploughing regimes. Thus $L_c^{(2)}$ can be interpreted physically as a critical contact length at which wear takes place. It is easy to obtain according to Figure 15 that the shearing stress of the present sliding system in the adhering regime, $\tau = F_x/(L_c w_a)$, is in the range of 0.7 GPa to 1.5 GPa. With so few dislocations activated in the atomic lattice, it is reasonable to see that τ is close to the theoretical shearing stress of a perfect copper monocrystal, which is $G/2\pi$ ($\approx$7.32 GPa) $\ge \tau_{theoretical} \ge G/30$ ($\approx$1.53 GPa),[40] where $G \approx 46$ GPa is the shear modulus of copper.

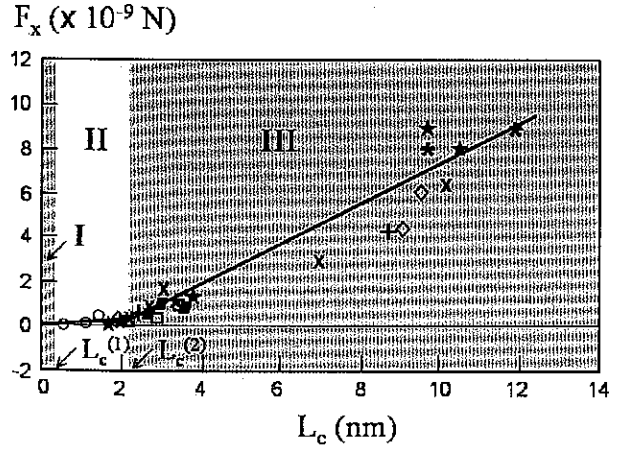

Fig. 15. Relationship between the frictional force and contact length. ×: $R = 5$ nm, $V = 20$ m/s, $\lambda_1 = 1$; ∗: $R = 5$ nm, $V = 100$ m/s, $\lambda_1 = 1$; ★: $R = 5$ nm, $V = 200$ m/s, $\lambda_1 = 1$; ○: $R = 1$ nm, $V = 200$ m/s, $\lambda_1 = 1$; ◇: $R = 5$ nm, $V = 200$ m/s, $\lambda_1 = 0.5$; ■: $R = 5$ nm, $V = 200$ m/s, $\lambda_1 = 0.6$; +: $R = 5$ nm, $V = 200$ m/s, $\lambda_1 = 0.7$; □: $R = 5$ nm, $V = 200$ m/s, $\lambda_1 = 0.8$. Reprinted with permission from [14], L. C. Zhang and H. Tanaka, *Wear* 211, 44 (**1997**). © 1997, Elsevier Science.

The linear equations, Eqs. (11b) and (11c) are only the rough fittings to the theoretical results. The data scattering in Figure 15 indicates that other variables, such as the tip radius of asperity R and sliding speed V, also contribute greatly to friction. In other words, F_x should be a function of not only the contact area $L_c w_a$ but also V, R, and so on.

It is worth to note from Figure 14 that the frictional force F_x does not vanish under a stable condition even if the system is in non-contact sliding. It is understandable since the interactions between the diamond and copper atoms always exist. In contact sliding with a small indentation depth, F_x remains small until a ploughing or a cutting is achieved. Hence, the frictionless sliding mentioned by Belak and Stowers[33] is doubtable. Indeed, in their simulation the indentation motion stopped after 2000 time steps but the 'frictionless motion' ended at the 1000 time step. In that period of time, sliding was still at the very initial transient state. Thus the variation of F_x with the time step of MD simulation does not make sense in terms of the frictional or frictionless sliding. In addition, the normal force variation that they reported is inconsistent with the indentation motion.

In summary, the molecular dynamics analysis has acquired the following important understandings of nano-wear and nano-friction on diamond-copper sliding systems:

(1) There exist four regimes of deformation in general in an atomic sliding system. They are the no-wear regime that is defect-free, adhering regime in which surface atom exchange occurs, ploughing regime that is characterised by a moving triangular atom-cluster, and cutting regime that material removal takes place.

(2) In the cutting regime, the frictional force follows the simple proportional rule of $F_x = \mu F_y$. In all the other regimes, the formulae in Eq. (11) apply.

(3) The transition between different deformation regimes are governed by indentation depth, sliding speed, asperity geometry and surface lubrication conditions. A better lubrication, a smaller tip radius, or a smaller sliding speed can bring about a greater no-wear regime and no-wear designs may be achieved in practice.

REVIEW

3.4. Scale Effect of Contact Size on Friction Transition

3.4.1. Introduction

The investigation by Zhang and Tanaka[14] described above focused on the friction and wear mechanisms when the radius of the asperity R is a constant while the depth of asperity indentation δ increases. Wear and plastic deformation consequently occur when δ reaches to a critical value.

Based on certain experimental observations,[42,43] Hurtado and Kim[44] proposed a micro-mechanical dislocation model of frictional slip, predicting that when the contact size is small the friction stress is constant and of the order of the theoretical shear strength. However, at a critical contact size there is a transition beyond which the frictional stress decreases with increasing contact size, until it reaches a second transition where the friction stress gradually becomes independent of the contact size. Hence, the mechanisms of slip are size-dependent, or in other words, there exists a scale effect. Before the first transition, the constant friction is associated with concurrent slip of the atoms without the aid of dislocation motion. The first transition corresponds to the minimum contact size at which a single dislocation loop is nucleated and sweeps through the whole contact interface, resulting in a single-dislocation-assisted slip. This mechanism is predicted to prevail for a wide range of contact sizes, from 10 nm to 10 μm, in radius for typical dry adhesive contacts; however, there are no available experimental data in this size range. The second transition occurs for contact sizes larger than 10 μm, beyond which friction stress is once again constant due to cooperative glide of dislocations within dislocation pileups. The above dislocation model excludes wear or plastic deformation of the sliding parts.

To clarify this issue, Zhang, Johnson and Cheong[24] carried out a nano-tribology analysis using molecular dynamics by varying the asperity radius from 5 nm to 30 nm and keeping the indentation depth unchanged. The model consists of a single cylindrical asperity (rigid diamond) of various radii, sliding across a copper (111) plane with a speed of 5 m/s. The indentation depth, d, was 0.46 nm and -0.14 nm (0.14 nm above the workpiece), respectively, where d is the distance between the surfaces of the asperity and specimen defined by the envelopes at the theoretical radii of their surface atoms. As usual, two layers of thermostat atoms are arranged around the Newtonian copper atoms of the specimen to ensure that the heat generated during sliding can conduct out of the control volume properly. The velocities of atoms in the initial configuration of the model follow the Maxwell distribution. The modified Morse potential, Eq. (9), was applied to describe the interactions between the atoms. It must be noted that the molecular dynamics simulation cannot capture the second transition because it will require too long a computation time to analyze a model in the order of micrometers.

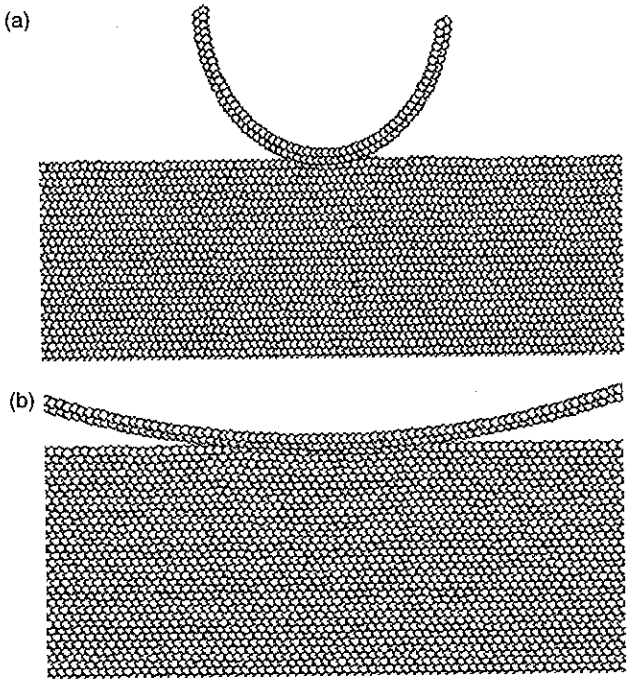

Fig. 16. Snapshots of sliding simulation with diamond asperities of different tip radius. (a) radius = 5 nm and (b) radius = 30 nm. Reprinted with permission from [24], L. C. Zhang et al., *Tribol. Lett.* 10, 23 (**2001**). © 2001, Springer Publishers.

3.4.2. Friction Transition

Figure 16 shows snapshots of the simulation with different asperity sizes. It is clear that the depths of indentation in the simulations are small enough so that there are no dislocations created within copper, corresponding to the no-wear regime described by Zhang and Tanaka.[14]

In the case where radius of the diamond asperity is less than 12 nm, the carbon atoms slide across the copper atoms in close contact. The surface of the copper workpiece conforms closely to the shape of the asperity tip in contact (Fig. 17(a)). There is also strong indication of atomic stick-slip between the atoms of the asperity and the workpiece (Fig. 17(b)). This implies that the sliding mechanism involved is similar to the ideal slip of two atomic planes in a perfect dislocation-free crystal. Hurtado and Kim[44] referred to this sliding mechanism as concurrent slip. In addition, the friction stress averages around a constant value of 5GPa regardless of the contact width (Fig. 19).

When the asperity radius exceeds 12 nm, there are considerable differences in the sliding mechanism involved. The surface of the copper workpiece does not conform closely to the shape of the carbon asperity (Fig. 18(a)). And there is little atomic stick-slip between the atoms of the asperity and the workpiece (Fig. 18(b)). In addition to that, the frictional stress now decreases with increasing the

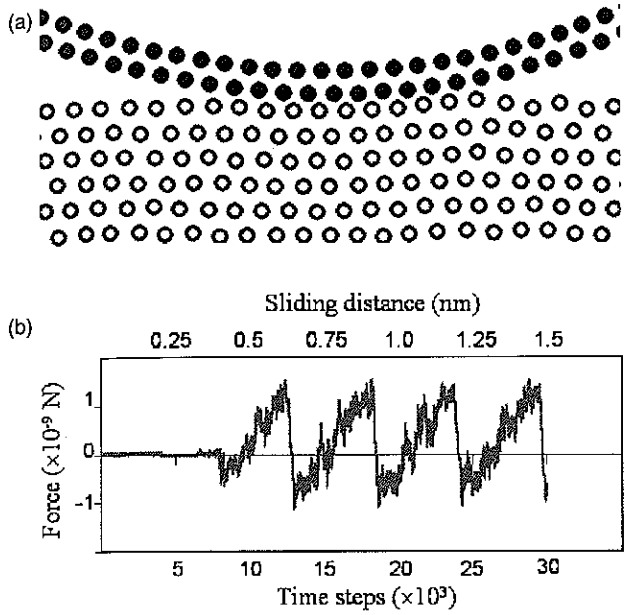

Fig. 17. Diamond asperity of radius 8 nm sliding on a monocrystalline copper surface. (a) Surface of copper workpiece conforms closely to shape of asperity with good contact and (b) Stick-slip phenomenon in sliding. Reprinted with permission from [24], L. C. Zhang et al., *Tribol. Lett.* 10, 23 (**2001**). © 2001, Springer Publishers.

contact width (Fig. 19). Hence, the friction stress is constant before the first transition but after which it decreases with the increasing contact width (by increasing the asperity radius). This clearly indicates a change in the mechanism of sliding.

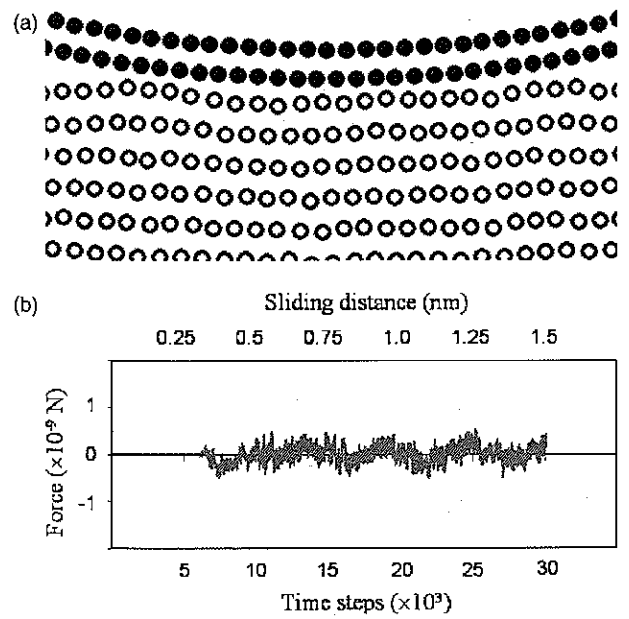

Fig. 18. Diamond asperity of radius 30 nm sliding on a monocrystalline copper surface. (a) Surface of copper workpiece does not conform closely to the shape of the asperity and (b) No stick-slip phenomenon in sliding. Reprinted with permission from [24], L. C. Zhang et al., *Tribol. Lett.* 10, 23 (**2001**). © 2001, Springer Publishers.

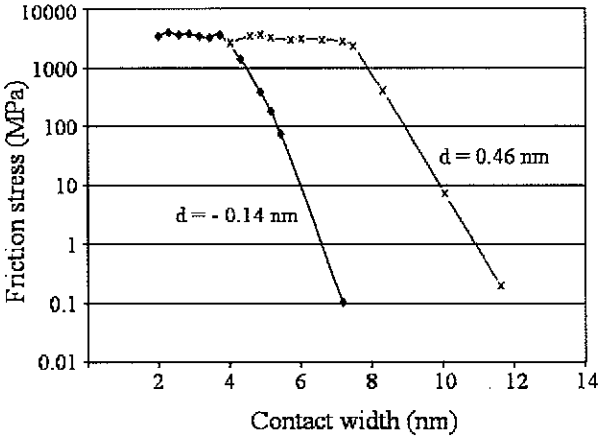

Fig. 19. Frictional Stress versus contact width for indentation depths of −0.14 nm and 0.46 nm. Reprinted with permission from [24], L. C. Zhang et al., *Tribol. Lett.* 10, 23 (**2001**). © 2001, Springer Publishers.

When the depth of indentation is increased to 0.46 nm, a somewhat similar relationship between friction stress and contact width is obtained. Figure 19 compares the variation of the friction stress and the critical contact width at the first transition when the indentation depth changes. It is clear that the indentation depth influences both the critical contact size and the rate of friction reduction after the transition. At this greater indentation depth, however, Figure 20 shows that permanent damage and wear are occurring. Dislocation lines indicating plastic deformation '*within the body of the solid*' are visible. This behavior is similar to the adhering regime described by Zhang and Tanaka.[14]

3.4.3. Contact Width

The contact width between the asperity and workpiece obtained by the above molecular dynamics simulation can be compared with the predictions of the JKR theory,[36,37] which shows, for the present configuration of a circular

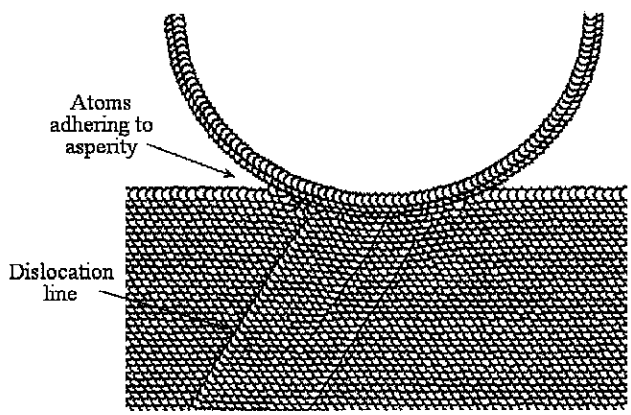

Fig. 20. Sliding simulation with indentation depth 0.46 nm and asperity radius 5 nm. Reprinted with permission from [24], L. C. Zhang et al., *Tribol. Lett.* 10, 23 (**2001**). © 2001, Springer Publishers.

Table IV. Contact lengths by the JKR and MD analyses for the case of diamond-copper interactions.

		Contact length 2a (nm)	
		$d = -0.14$ nm, $P = 0.625$ N/m	$d = 0.46$ nm, $P = 22.969$ N/m
$R = 5$ nm	JKR	2.914	3.764
	MD	2.870	4.120
	Hertz	0	2.160
		$d = -0.14$ nm, $P = 0.824$ N/m	$d = 0.46$ nm, $P = 27.34$ N/m
$R = 8$ nm	JKR	3.99	5.152
	MD	3.731	5.740
	Hertz	0	2.980

cylinder in contact with a half space (plane-strain), that the indentation load per unit width on the asperity, P, and the contact width, 2a, follows the relationship of

$$P = \frac{\pi E^* a^2}{4R} - \sqrt{2\pi E^* a w} \tag{12}$$

where R is the radius of the asperity, E^* is the effective modulus of the contact system,[36] w is the work of adhesion and can be determined by a nano-indentation simulation using molecular dynamics analysis. It is found that for the present diamond-copper (C–Cu) system, $w_{C-Cu} = 1.476$ J/m^2. Since the diamond asperity is assumed to be a rigid body, the E^* in Eq. (12) becomes 125.36 GPa by taking $E_C = \infty$, $E_{Cu} = 110$ GPa and $\nu_{Cu} = 0.35$.[45]

Table IV compares the contact widths from the molecular dynamics simulation, the JKR theory of Eq. (12) and the Hertzian contact theory under various conditions. The values from the JKR and simulation are different, although the deformation of the copper workpiece at $d = -0.14$ nm was purely elastic and that at $d = 0.46$ nm was almost purely elastic. A possible cause is that the contact width of the molecular dynamics simulation contains the effect of sliding, while Eq. (12) does not. It is also worth noting that the predictions by the JKR theory compared to the predictions by the Hertzian contact theory is much closer to the molecular dynamics results. This indicates that the effect of normal adhesion is considerable.

In calculating the contact width above using Eq. (12), the force P used is from the corresponding molecular dynamics simulation as listed in the table. In their paper,[24] Zhang, Johnson, and Cheong also discussed the sliding on copper by a copper asperity.

3.4.4. Mechanism—An Open Question

Apparently, the above result of molecular dynamics simulation is in agreement with the phenomenon predicted by the dislocation model,[44] but the mechanisms are different. A quantitative comparison between the predictions of the two modelling methods is worthwhile, although the specimen materials are different and the dislocation

Table V. Comparisons of dimensionless shear stress (τ/μ) and contact size (a/b) at transition.

	2-D MD model		
	$d = -0.14$ nm	$d = 0.46$ nm	3-D Theoretical model
τ/μ	0.061	0.037	0.023
a/b	6.53	13.06	30
ξ (Pa/m)	2.90×10^{18}	1.46×10^{18}	1.88×10^{13}

model is three-dimensional whereas the present molecular dynamics simulation is two-dimensional. Table V shows the results of the dislocation model and those of the molecular dynamics simulation. The value of τ/μ obtained from the molecular dynamics simulation is close, particularly in the case of $d = 0.46$ nm, to that of the dislocation model, where τ is the shear stress and μ is the bulk shear modulus defined by Hurtado and Kim[44] as $\mu = 2G_1G_2/(G_1 + G_2)$ in which G_1 is the shear modulus of the asperity and G_2 is that of the copper specimen. In the present molecular dynamics simulation, the asperity is rigid so that $G_1 = \infty$ and $\mu = 2G_2 = 81.48$ GPa. The ratio a/b at the transition varies considerably with the indentation depth, where a is half of the critical contact width and b is the Burgers vector. The ratio for the case of $d = 0.46$ nm is closer to that of the dislocation model. However, it is interesting to note that in the transition zone the rates of friction reduction with the contact size, $\xi = d\tau/da$, are very different. The molecular dynamics analysis gives a much greater rate. A better understanding is needed by using a three dimensional model.

The above analysis concludes that there does exist a critical contact size on the nanometer scale, below which the 'stick-slip' occurs and sliding occurs by concurrent slip of all the atoms in the contact at a friction of the theoretical shear strength of the solid. When the contact size is beyound the critical value, a friction transition takes place to a much lower value. The critical contact size varies with the degree of penetration of the asperity. In addition, the study fuher confirms that the Hertz theory fails to predict the contact size in vacuum at the nanometer scale when surface energy plays a key role.

Recently, Mulliah et al.[46] proposed a spring model to investigate the stick-slip phenomenon for a pyramidal diamond tip in contact with (010) fcc silver surface. They investigated the mechanism by considering different sliding speeds and vertical displacements. For small vertical displacement, they found that the scratch was not continious whereas for large vertical displacement the scratch was continious. At small displacement the stick-slip was revealed by the calculated static friction coefficient values which were three times larger than the dynamics values. For large displacement, the static and dynamics friction coefficient values were close to each other and the stick-slip was manifested by periods of motion where the tip moved faster and then slower than the support.

3.5. Diamond-Silicon Sliding Systems

3.5.1. Modelling

Let us now consider the two-body and three-body contact sliding problems defined in Figure 6. In the former, asperities are fixed on the sliding surfaces. To understand the fundamental deformation mechanism in a component induced by the penetration of asperities, a molecular dynamics model illustrated in Figure 6(a) is developed,[16] where the shape of a hard asperity, which should be irregular in reality, has been simplified to a hemispherical diamond tip of radius R moving with a constant speed V_c. Since a diamond can be considered as a rigid body compared with silicon, the model enables us to concentrate on the understanding of deformation of silicon. In a three-body contact sliding, the model shown in Figure 6(b)[16] can be used, where the motion of a foreign particle between the two surfaces possesses both a translation and a self-rotation. To facilitate understanding, a single particle is considered for the time being and is approximated by a diamond ball of radius R, moving horizontally (translation) with a speed V_c and in the meantime rotating about its centre independently with a peripheral speed V_r. When $V_r = 0$, the three-body contact sliding reduces to a two-body one. When $V_c = 0$ or $V_r = V_c$, on the other hand, it becomes a pure rolling process. To avoid the boundary effect, the dimension of the moving control volume of the silicon specimen was taken as 9.23 (nm) × 13.57 (nm) × 4.34 (nm), containing 28,773 silicon atoms.

3.5.2. Inelastic Deformation

The molecular dynamics simulation showed that there always exists a thin layer of amorphous silicon in a specimen subsurface subjected to a two-body contact sliding, as shown in Figure 21(a). This is in agreement with the experimental findings by Zhang and Zarudi[47] (Fig. 21(b)). The thickness of the layer decreases with decreasing the penetration depth of asperity (Fig. 21(c)), δ. If δ is large (e.g., 763 nm), dislocations can be developed in the crystal silicon below the amorphous layer. When δ becomes smaller, dislocations cannot be activated but the amorphous layer still appears. This means that on the nanometer scale an inelastic deformation via amorphous phase transformation is a more energetically favourable mechanism. In the case with three-body contact sliding, the mechanism of inelastic deformation is the same, i.e., via amorphous phase transformation. However, because of the kinetic difference in the two-body and three-body sliding motions, the extent of subsurface damage is different. In general, a two-body contact sliding introduces a thinner layer of amorphous. A three-body contact sliding, however, may leave a perfect crystal structure after sliding although wear has happened, depending on the penetration depth of the particle, its speed ratio of self-rotation to translation and variation of atomic bonding strength affected by surface

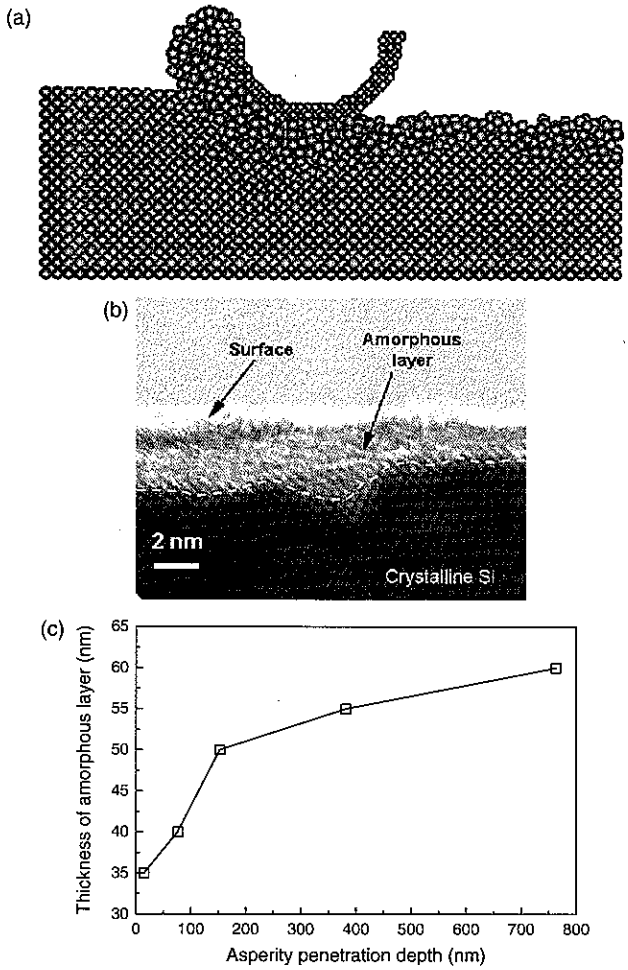

Fig. 21. The subsurface microstructure of silicon monocrystals after a two-body contact sliding. The amorphous phase transformation has been predicted. (a) a cross-sectional view of the deformed subsurface of the specimen ($V_c = 200$ m/s, $R = 2.1$ nm, $d = 0.99$ nm, sliding in [100] direction). Reprinted with permission from [16], L. C. Zhang and H. Tanaka, *Tribol. Int.* 31, 425 **(1998)**. © 1998, Elsevier Science. (b) an experimental result of the subsurface damage induced. Note the top amorphous layer. ($V_c = 23.95$ m/s, $R = 1$ μm, $d = 15.2$ nm, sliding in [100] direction) Here, each spot represents a silicon atom. Reprinted with permission from [47], L. C. Zhang and I. Zarudi, *Int. J. Mech. Sci.* 43, 1985 **(2001)**. © 2001, Elsevier Science. (c) experimentally measured thickness variation of amorphous layer with the indentation depth of the asperity ($V_c = 23.95$ m/s, $R = 1$ μm, sliding in [100] direction. Reprinted with permission from [16], L. C. Zhang and H. Tanaka, *Tribol. Int.* 31, 425 **(1998)**. © 1998, Elsevier Science.

contamination. It was also found that the variation of sliding velocity from 20 m/s to 200 m/s does not change the deformation mechanisms described above.

Figure 22(a) is a molecular dynamics prediction on the deformation caused by a three-body contact sliding. It is clear that at location ⟨2–4⟩ specified in the figure, the shape of the crystal-amorphous boundary is irregular; but at location ⟨1–3⟩, the boundary is mostly regular along the (111) atomic lattice orientation. This coincides very well with the experimental findings reported by Zarudi et al.[48] shown in Figure 22(b) to Figure 22(d). According to the

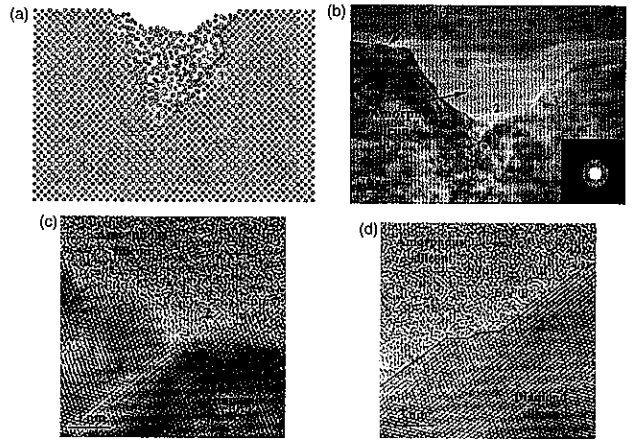

Fig. 22. Comparison of theoretical prediction and experimental observation. In (c) and (d), each spot represents a silicon atom observed in experiment. (a) Molecular dynamics prediction of the deformation in the scratch generated by nanopolishing (a) cross-sectional view, (b) A cross-sectional view of the deformation in a scratch generated by nanopolishing (experiment), (c) The atomic orientations at the boundary (location ⟨2–4⟩), and (d) The atomic orientations at the boundary (location ⟨1–3⟩). Reprinted with permission from [48], I. Zarudi et al., *Nanotechnology* 15, 104 **(2004)**. © 2004, IOP Publishing Ltd.

theory of contact mechanics, the stress fields at locations ⟨2–4⟩ and ⟨1–3⟩ are different. At the former, the hydrostatic stress component dominates so that the boundary does not go along a single atomic lattice orientation. At the latter, however, the shear stresses play a central role and hence the phase change terminates in a particular orientation. These are aligned with the stress criteria for various phase transformation events in silicon proposed.[15,49]

3.5.3. *Wear Regimes*

Similar to the wear mechanisms for the diamond-copper sliding system[14] discussed previously, the wear regimes of the current diamond-silicon system also depend on sliding conditions, as shown by the mechanism diagram, Figure 23. In a two-body contact sliding with a given sliding speed, the deformation of a silicon monocrystal falls into *no-wear*, *adhering*, *ploughing*, or *cutting* regime when the asperity penetration depth varies, see the left half of the figure. Deformation without wear happens only under an extremely small penetration depth, when the atomic lattice of silicon deforms purely elastically. With increasing the penetration depth, adhering takes place (Fig. 24(a)), in which some surface atoms stick to the asperity surface and move together with it to cause wear. However, these atoms may return to the silicon substrate during sliding if the specimen surface has not been contaminated. When the penetration depth increases further, a new wear state, ploughing, characterised by an atomic cluster being pushed to move with the asperity, will appear (Fig. 24(b)). A further increase of the penetration depth leads to a continuous cutting process.

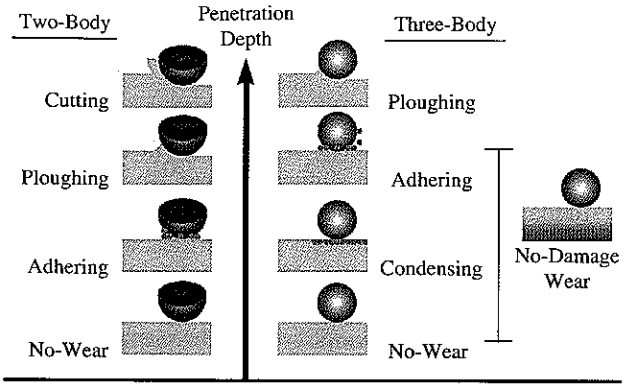

Fig. 23. The wear diagram. The diamond asperities/particles move from the right to the left. The rotation of particles is anticlockwise. Reprinted with permission from [16], L. C. Zhang and H. Tanaka, *Tribol. Int.* 31, 425 **(1998)**. © 1998, Elsevier Science.

In a three-body contact sliding, however, silicon will experience different wear regimes. They are the *no-wear*, *condensing*, *adhering*, and *ploughing* regimes, as shown in the right half of Figure 23. After the pure elastic deformation in the no-wear regime, the amorphous phase under the particle will experience a remarkable condensing locally without material removal. In other words, because the density of the surface silicon atoms under particle indentation becomes higher, condensing creates a sliding mark on the specimen surface, see Figure 25(a). Thus condensing is a special wear process without material removal. A further particle penetration will lead to adhering and ploughing (Fig. 25(b)). These regimes are similar to the

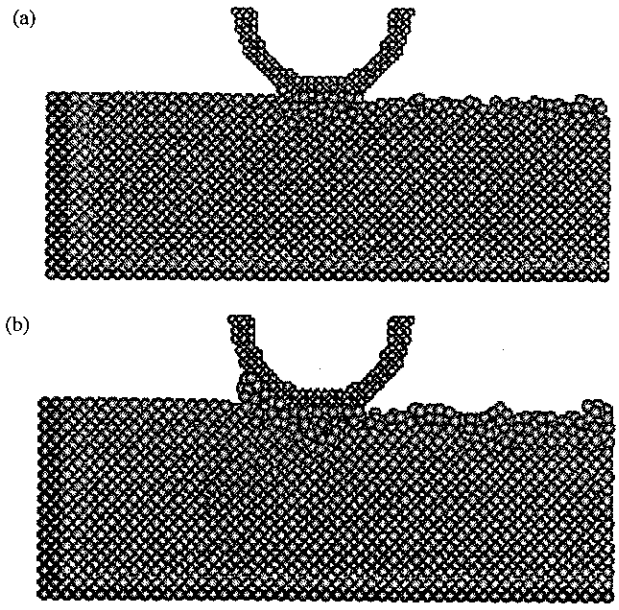

Fig. 24. Characteristics of various deformation regimes in two-body contact sliding processes (a cross-sectional view). ($V_c = 200$ m/s, $R =$ 2.1 nm, sliding in [100] direction) (a) adhering ($d = 0.19$ nm) and (b) ploughing ($d = 0.39$ nm). Reprinted with permission from [16], L. C. Zhang and H. Tanaka, *Tribol. Int.* 31, 425 **(1998)**. © 1998, Elsevier Science.

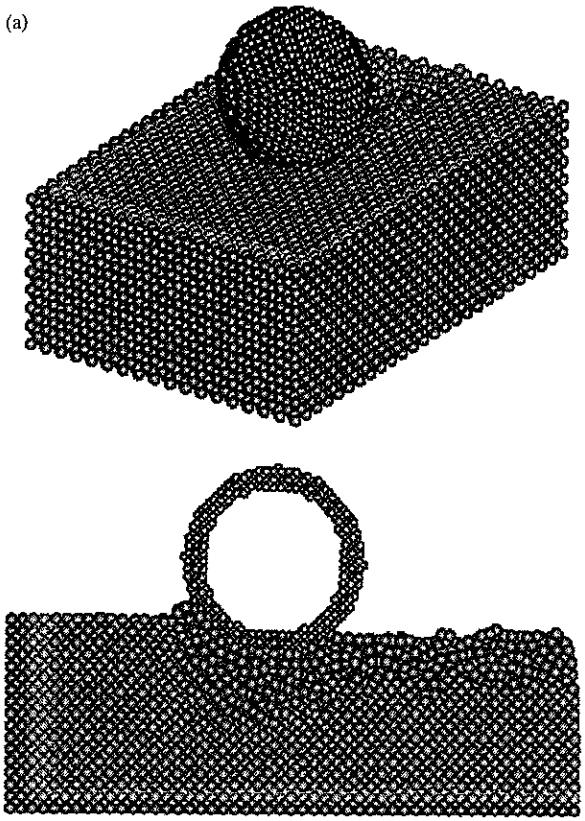

Fig. 25. Deformation regimes associated with three-body contact sliding—a cross-sectional view. ($V_c = 200$ m/s, $V_r = 100$ m/s, $R = 2.1$ nm, sliding in [100] direction) (a) condensing ($d = 0.19$ nm) and (b) ploughing ($d = 0.99$ nm). Reprinted with permission from [16], L. C. Zhang and H. Tanaka, *Tribol. Int.* 31, 425 **(1998)**. © 1998, Elsevier Science.

corresponding ones in the two-body contact sliding. Cutting rarely happens in three-body sliding processes but is possible if the particle penetration depth becomes sufficiently large and the self-rotation speed becomes small.

Another interesting phenomenon associated with the three-body contact sliding is the existence of a regime of *no-damage wear*. Under certain sliding conditions, the atomic bonding strength among surface silicon atoms can be weakened chemically. When this happens, these atoms can be removed via adhesion because diamond-silicon attraction is still strong, as shown in Figure 26. Due to the re-crystallisation behind the particle, a worn specimen may appear as damage-free in the majority of its subsurface with only little distortion within one or two surface atomic layers. In conjunction with the phenomenon happened in the condensing regime discussed above, it becomes obvious that a perfect subsurface after a three-body contact sliding does not necessarily indicate a no-wear process.

3.6. Multi-Asperity Sliding

3.6.1. *Modelling*

Previous study of a single sliding asperity has provided us with important knowledge on the deformation mechanisms

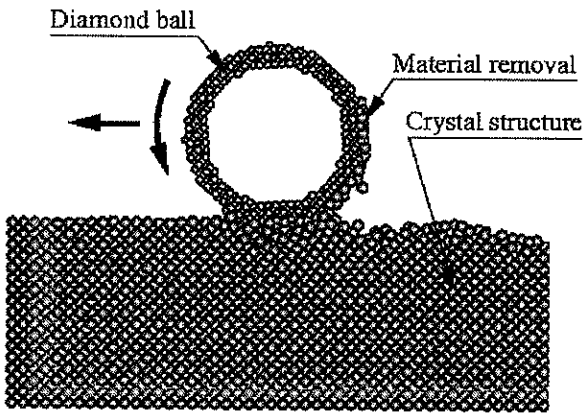

Fig. 26. Material removal via adhering in a three-body sliding process when the C–Si interaction is three times stronger than that of Si–Si. The particle translation is from the right to the left and its rotation is anticlockwise. ($V_c = 200$ m/s, $V_r = 100$ m/s, $R = 2.1$ nm and $d = 0.19$ nm). Reprinted with permission from [16], L. C. Zhang and H. Tanaka, *Tribol. Int.* 31, 425 **(1998)**. © 1998, Elsevier Science.

of friction and wear of monocrystalline materials. In a real sliding system, however, a counterpart material is actually subjected to multi-asperity interactions, as illustrated in the inserts of Figures 6(a) and 6(b). When the first asperity has created a damaged zone, the material may deform differently under subsequent sliding interactions. Cheong and Zhang thus discussed the effects of the sliding by multi-asperities.[50]

The mechanics model consists of three spherical diamond asperities, A, B, and C, sliding on an atomically smooth silicon surface, as illustrated in Figure 27. Their relative positions and orientations are defined by their distances, L_{AB} and L_{AC}, and angles with respect to the sliding direction, α and θ. Three cases are of special interest, which are (I) $\alpha = \theta = 0°$ with $L_{AB} < L_{AC}$, representing a repeated single-asperity sliding so that the effect of residual subsurface damage can be understood, (II) $\alpha = 0°$ and $\theta = 90°$ with $L_{AB} = L_{AC}$, standing for the interaction of two parallel asperities, and (III) $\alpha = 90°$ and $\theta = 0°$, indicating the case with parallel sliding asperities coupled with an interaction from a third asperity. Again, since diamond is much harder than silicon, the asperities are modeled as rigid spheres. These spheres slide across the silicon surface

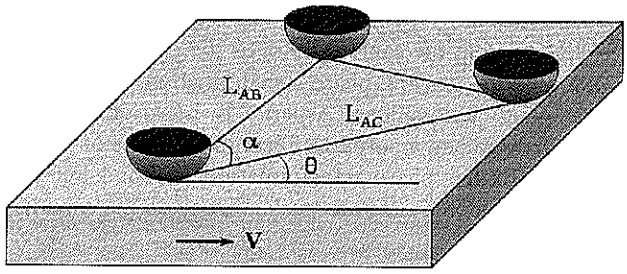

Fig. 27. The mechanics model for multi-asperity contact sliding. Reprinted with permission from [50], W. C. D. Cheong and L. C. Zhang, *Int. J. Materials and Product Tech.* 18, 398 **(2003)**. © 2003, Inderscience Publishers.

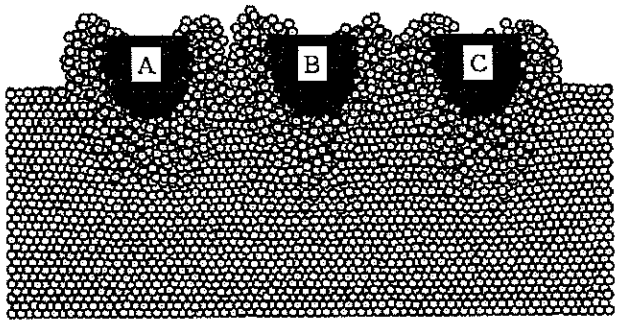

Fig. 28. Cross-section of the silicon workpiece through the center of asperities. Reprinted with permission from [50], W. C. D. Cheong and L. C. Zhang, *Int. J. Materials and Product Tech.* 18, 398 **(2003)**. © 2003, Inderscience Publishers.

at a specified velocity 40 m/s. The maximum depth of asperity penetration is 1.0 nm.

3.6.2. Configuration II and III

In the cases of configurations II and III, the asperities do not retrace the damaged zones. At the depth of asperity penetration of 1.0 nm, the wear mechanism observed is that of cutting. The plastic deformation due to the sliding asperities is very localized. Figure 28 shows a cross-section of the silicon workpiece through the centre of the asperities. It can be seen that there is almost no subsurface damage to the silicon workpiece between the two asperities. Plastic deformation is very localized and occurs beneath the asperities.

As in nano-indentation,[51] the sliding asperities A, B, and C also create trails of subsurface amorphous layer in the damaged zones. Phase transformation of silicon occurs at the leading edge beneath the sliding asperity resulting in the formation of amorphous chips and an amorphous trail along the path traversed by the asperities. Dislocations are absent at this particular depth of asperity penetration. This suggests that the plastic deformation is solely due to phase transformation.

3.6.3. Configuration I

In this case, the second and third asperities B and C retrace the damaged path caused by asperity A. Therefore, the cutting mechanism involved in the first and the following two asperities are very different. Asperity A cuts the silicon workpiece in the same fashion as the case of a single sliding asperity, causing phase transformation of the original diamond cubic silicon. Asperity B, however, ploughs through the residual amorphous layer in the wake of asperity A. No further phase transformation is found but the amorphous silicon atoms are pushed away as the asperity ploughs through.

3.6.4. Phase Transformation

As shown above, something apparent in the silicon workpiece in all the three configurations is the formation of

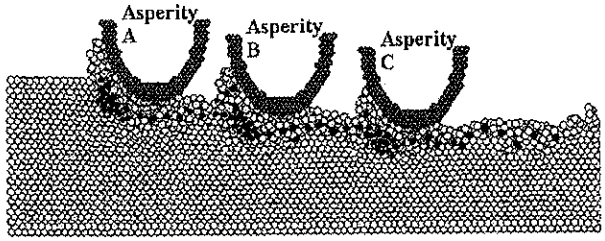

Fig. 29. Cross-sectional view of asperities A, B, and C in configuration I. A light coloured circle represents an atom with coordination number 4 and a dark circle represents an atom with coordination number 6. Reprinted with permission from [50], W. C. D. Cheong and L. C. Zhang, *Int. J. Materials and Product Tech.* 18, 398 **(2003)**. © 2003, Inderscience Publishers.

an amorphous subsurface layer in regions traversed by the diamond asperities. This is analogous to the amorphous damaged zone due to nano-indentation. Hence it is worthwhile to draw comparisons and to predict the process of phase transformation based on results obtained from nano-indentation.[15, 51]

With configurations II and III, wear via cutting is achieved by chipping the amorphous silicon. By considering the exact coordinates of the silicon atoms, it is found that the transformation mechanism is similar to that of nano-indentation.[51] Diamond cubic silicon first transforms into its β-tin phase and then upon the removal of stresses, transforms into an amorphous phase. This explains the trail of subsurface amorphous silicon in the damaged zone behind each sliding asperity. The mechanism of phase transformation is reflected in the coordination numbers of atoms near the regions beneath the asperities. It can be seen that a cluster of six-coordinated body-centred tetragonal β-tin silicon atoms indicated by darken circles (Fig. 29) forms near the leading edge beneath each asperity. Four-coordinated diamond cubic silicon transforms to its six-coordinated β-tin form due to the stresses induced by the asperity. When the stresses are removed as the asperity slides past, the atoms transforms into an energetically more favourable amorphous form. The coordination number of the silicon atoms in the trailing amorphous region is mostly equal to four. Therefore, as the asperity slides across the silicon workpiece, diamond cubic silicon continuously transforms into β-tin silicon beneath the asperity and then transforms into amorphous silicon when the asperity passes, leaving a layer of subsurface amorphous silicon in its wake.

Figure 30 shows the number of β-tin silicon atoms formed during the cutting process with asperity configurations II and III. The number of β-tin silicon in configurations II and III are three times that of a single asperity cutting process. This indicates that the formation of β-tin silicon is highly stress state dependent and occurs only beneath the three asperities. Although regions between the asperities are compressed due to the proximity of the asperities, it is likely that β-tin silicon do not form because of the absence of the required stress states.

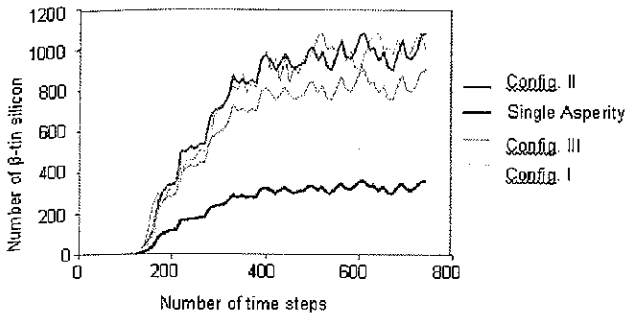

Fig. 30. The number of 6-coordinated β-tin silicon atoms in Configurations I, II, and III compared to that with a single asperity. Reprinted with permission from [50], W. C. D. Cheong and L. C. Zhang, *Int. J. Materials and Product Tech.* 18, 398 (**2003**). © 2003, Inderscience Publishers.

With Configuration I, asperity A cuts the silicon workpiece in very much the same way as in the other two configurations described above. The asperity cuts through the diamond cubic silicon leaving behind a trail of subsurface amorphous silicon. However there is a vast difference in the silicon phase transformation involved due to asperities B and C, which represent subsequent cuts into the amorphous zone. In the present case, the six-coordinated atoms also form beneath asperities B and C (Fig. 29). This implies that the β-tin silicon phase is recoverable from the amorphous phase provided that the required stress field is achieved. It must be noted that only some of the β-tin silicon is recovered as asperity B and C retraces the amorphous damaged zone. That is why the number of β-tin silicon atoms in Configuration I is slightly less than that of Configuration II and II (Fig. 30).

4. CONCLUSION

This review has discussed some fundamental issues in studying the nano-tribology using molecular dynamics, such as adhesion, wear, and friction, and the mechanisms, involved in the diamond-copper and diamond-silicon sliding systems. The understanding achieved is very useful to the development of products with good performance and durability.

Acknowledgment: The research presented in this paper has been supported by many research grants, including the ARC (Large, IREX, Fellowship, Discovery) and the University of Sydney Research Grants.

References

1. D. Dowson, *History of Tribology*, Longman Group Ltd., London (**1979**).
2. K. Kendall, *Science* 263, 1720 (**1994**).
3. C. H. Mastrangelo, *Tribol. Lett.* 3, 223 (**1997**).
4. J. Ruan and B. Bhushan, *J. Appl. Phys.* 76, 5022 (**1994**).
5. B. Bhushan, *Tribol. Int.* 28, 85 (**1995**).
6. V. N. Koinkar and B. Bhushan, *J. Appl. Phys.* 81, 2472 (**1997**).
7. S. Sundararajan and B. Bhushan, *J. Appl. Phys.* 88, 4825 (**2000**).
8. B. Bhushan and S. Sundararajan, *Acta Mater.* 46, 3793 (**1998**).
9. B. Bhushan and C. Dandavate, *J. Appl. Phys.* 87, 1201 (**2000**).
10. X. Zhao and B. Bhushan, *Wear* 223, 66 (**1998**).
11. B. Bhushan and J. Ruan, *ASME J. Trib.* 116, 389 (**1994**).
12. B. Bhushan, *Wear* 259, 1507 (**2005**).
13. J. M. Haile, *Molecular Dynamics Simualtion*, John Wiley and Sons Inc., New York (**1992**).
14. L. C. Zhang and H. Tanaka, *Wear* 211, 44 (**1997**).
15. L. C. Zhang and H. Tanaka, *JSME Int. J. Series A* 42, 546 (**1999**).
16. L. C. Zhang and H. Tanaka, *Tribol. Int.* 31, 425 (**1998**).
17. L. C. Zhang, D. Cheong, and H. Tanaka, in *Abrasive Technology: Current Development and Appplications*, edited by J. Wang, W. Scott, and L. C. Zhang, World Scientific, Singapore (**1999**), p. 407.
18. J. Tersoff, *Phys. Rev. Lett.* 56, 632 (**1986**).
19. J. Tersoff, *Phys. Rev. B* 39, 5566 (**1989**).
20. L. C. Zhang and H. Tanaka, in *Advances in Abrasive Technology*, edited by L. C. Zhang and N. Yasunaga, World Scientific, Singapore (**1997**), p. 43.
21. C. Kittel, *Introduction to Solid State Physics*, 7th Edn., John Wiley and Sons Inc., New York (**1996**).
22. L. C. Zhang, *Solid Mechanics for Engineers*, Palgrave, Malaysia (**2001**).
23. J. E. Inglesfield, *Potentials in Metals, Computer Simulation of Solids*, Springer-Verlag, New York (**1982**), p. 115.
24. L. C. Zhang, K. L. Johnson, and W. C. D. Cheong, *Tribol. Lett.* 10, 23 (**2001**).
25. C. M. Mate, G. M. McClelland, R. Erlandsson, and S. Chiang, *Phys. Rev. Lett.* 59, 1942 (**1987**).
26. R. Kaneko, *J. Vac. Sci. Tech.* A6, 291 (**1988**).
27. P. Bak, *Prog. Phys.* 45, 587 (**1982**).
28. W. Zhong, *Phys. Rev. Lett.* 64, 3054 (**1990**).
29. G. M. McClelland, in *Adhesion and Friction*, edited by H. J. Kreuzer and M. Grunze, Springer-Verlag, Berlin (**1989**), p. 1.
30. J. B. Sokoloff, *Surface Sci.* 144, 267 (**1984**).
31. U. Landman, *J. Vac. Sci. Tech.* 47, 2829 (**1989**).
32. D. Mulliah, S. D. Kenny, R. Smith, and C. F. Sanz-Navarro, *Nanotechnology* 15, 243 (**2004**).
33. J. Belak and I. F. Stowers, in *Fundamentals of Friction: Macroscopic and Microscopic Processes*, edited by I. L. Singer and H. M. Pollock, Kluwer Academic Publisher, Dordrecht (**1992**), p. 511.
34. A. M. Homola, *Wear* 136, 65 (**1990**).
35. F. P. Bowden and D. Tabor, *Friction and Lubrication*, Methuen, London (**1967**).
36. K. L. Johnson, Contact Mechanics, Cambridge University Press, Cambridge (**1985**).
37. K. L. Johnson, K. R. Kendall, and A. D. Roberts, *Proc. R. Soc. London A* 324, 301 (**1971**).
38. W. C. D. Cheong, L. C. Zhang, and H. Tanaka, *Key Engineering Materials* 196, 31 (**2001**).
39. H. Tanaka and L. C. Zhang, in *Progress of Cutting and Grinding*, edited by N. Narutaki, Japan Society for Precision Engineering, Osaka (**1996**), p. 262.
40. T. H. Courtney, *Mechanical Behaviour of Materials*, McGraw-Hill, Singapore (**1990**).
41. Y.-R. Jeng, P.-C. Tsai, and T.-H. Fang, *Nanotechnology* 16, 1941 (**2005**).
42. R. W. Carpick, D. F. Agrait, D. F. Ogletree, and M. Salmeron, *Langmuir* 12, 505 (**1996**).
43. M. A. Lantz, S. L. O'Shea, M. E. Welland, and K. L. Johnson, *Phys. Rev. B* 55, 10776 (**1997**).
44. J. A. Hurtado and K.-S. Kim, *Proc. R. Soc. London A* 455, 3363 (**1999**).
45. W. D. Callister, Jr., *Materials Science and Engineering—An Introduction*, 3rd edn., John Wiley and Sons, New York (**1995**), p. 767.

46. D. Mulliah, S. D. Kenny, and R. Smith, *Phys. Rev. B* 69, 205407 (**2004**).
47. L. C. Zhang and I. Zarudi, *Int. J. Mech. Sci.* 43, 1985 (**2001**).
48. I. Zarudi, W. C. D. Cheong, J. Zou, and L. C. Zhang, *Nanotechnology* 15, 104 (**2004**).
49. W. C. D. Cheong and L. C. Zhang, *Key Engineering Materials*, 233–236, 603 (**2003**).
50. W. C. D. Cheong and L. C. Zhang, *Int. J. Materials and Product Tech.* 18, 398 (**2003**).
51. W. C. D. Cheong and L. C. Zhang, *Nanotechnology* 11, 173 (**2000**).

Received: 22 December 2005. Accepted: 28 December 2005.